Transient Thermo-fluid Model of Meniscus Behavior and Slag Consumption in Steel Continuous Casting

ASM JONAYAT and BRIAN G. THOMAS

The behavior of the slag layer between the oscillating mold wall, the slag rim, the slag/liquid steel interface, and the solidifying steel shell, is of immense importance for the surface quality of continuous-cast steel. A computational model of the meniscus region has been developed, that includes transient heat transfer, multi-phase fluid flow, solidification of the slag, and movement of the mold during an oscillation cycle. First, the model is applied to a lab experiment done with a "mold simulator" to verify the transient temperature-field predictions. Next, the model is verified by matching with available literature and plant measurements of slag consumption. A reasonable agreement has been observed for both temperature and flow-field. The predictions show that transient temperature behavior depends on the location of the thermocouple during the oscillation relative to the meniscus. During an oscillation cycle, heat transfer variations in a laboratory frame of reference are more severe than experienced by the moving mold thermocouples, and the local heat transfer rate is increased greatly when steel overflows the meniscus. Finally, the model is applied to conduct a parametric study on the effect of casting speed, stroke, frequency, and modification ratio on slag consumption. Slag consumption per unit area increases with increase of stroke and modification ratio, and decreases with increase of casting speed while the relation with frequency is not straightforward. The match between model predictions and literature trends suggests that this methodology can be used for further investigations.

DOI: 10.1007/s11663-014-0097-9

I. INTRODUCTION

IN continuous casting of steel, initial solidification in the mold near the meniscus is very important to ultimate quality of the steel. Defects[1,2] arising near the meniscus remain at the surface of the eventual steel products, and are expensive or impossible to remove. To prevent oxidation of the molten steel by exposure to air, a layer of mold powder is maintained on the top surface by periodic additions of this carefully selected, proportioned, and mixed combination of metal oxide powders and graphite. This powder provides lubrication, maintains uniform heat transfer between the mold and steel shell, and removes inclusions that rise up from the molten steel.[3]

Figure 1(a) shows a schematic of the continuous casting process. Liquid steel flows from the tundish (not shown in figure) into the mold, through the submerged entry nozzle's (SEN) bifurcated ports that direct the flow of the molten liquid jets toward the narrow face mold walls and eventually upwards to the meniscus region at the top surface around the mold perimeter. Cooling water flows through the channels of the mold, and extracts heat, causing the superheated liquid steel to solidify against the mold walls as a shell or steel strand, which is pulled downward at the casting speed. To prevent sticking, the mold oscillates with a given frequency, stroke (2 × amplitude) and sometimes a modification ratio for non-sinusoidal oscillation.[4] During the casting process, the mold powder gets heated, sinters, and melts to form a molten slag layer that floats on top of the molten steel.[5] The shape of the interface between the slag and steel curves in the meniscus region, according to the surface tension, buoyancy, and momentum forces, and changes with time according to the mold oscillation and turbulent flow.[6,7] The liquid slag is eventually consumed into the thin gap between the mold and the solidifying steel shell by the downward movement of the strand. The amount of slag that has to be added to the mold surface over time is termed as slag consumption.

Figure 1(b) shows a close-up schematic of the phenomena near the meniscus at the mold hot face, where the molten slag transforms to solid slag as it cools due to heat removal into the water-cooled mold. As a result, the gap between the mold hot face and the steel shell contains slag in two phases—solid and liquid. A thicker layer of solid slag termed the "Slag Rim" solidifies against the mold hot face above the liquid slag layer.[8] The slag rim sticks to the mold and oscillates with it. In addition to affecting the heat flux, the oscillating slag rim periodically pushes on the liquid or partially solidified meniscus[9] which may form depressions on the steel shell surface called "Oscillation Marks (OM)".[3,10] Downward movement of the OMs also

---

ASM JONAYAT, Graduate Research Assistant, and BRIAN G. THOMAS, C.J. Gauthier Professor, are with the Department of Mechanical Science and Engineering, University of Illinois at Urbana-Champaign, 1206 West Green Street, Urbana, IL-61801. Contact e-mail: bgthomas@illinois.edu

Manuscript submitted April 26, 2014.

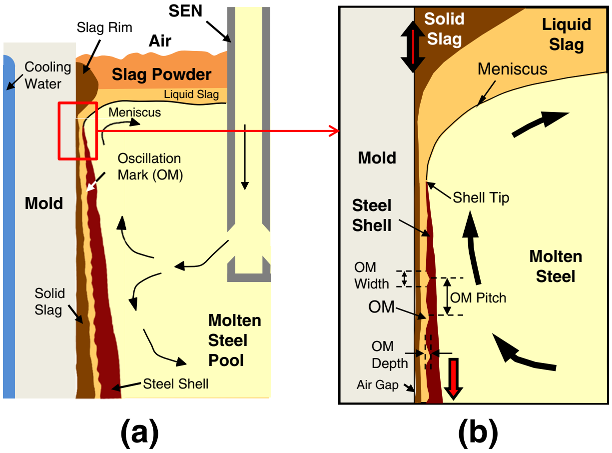

Fig. 1—(*a*) Transient phenomena in a caster (*b*) meniscus region.

consumes slag. The slag viscosity and other properties change greatly with temperature.[11] Furthermore, the melting powder has different properties than the cooling liquid slag, even at the same temperature.[12]

The slag must fulfill many important functions, in addition to preventing air oxidation. If the slag layer in the gap is not thick enough, the steel shell may come into direct contact with the mold wall, which may cause sticking of the steel eventually leading to a catastrophic breakout,[13] where molten steel escapes from a rupture in the shell below mold exit. If the inclusions that rise up are unable to be captured into the liquid slag layer, then many inclusions will end up in the final product. If heat flux variations near the meniscus are too severe, due to slag layer thickness variations, then cracks may form.[14–16] Finally, if fluctuations of the liquid steel/slag interface are too severe, then liquid slag may become entrained into the solid or molten steel, leading to surface or internal defects, respectively.[17,18]

Slag consumption is affected by many casting parameters—casting speed, oscillation frequency, stroke, and mode of oscillation (sinusoidal/non-sinusoidal).[19] The material properties also affect slag consumption. To optimize slag behavior in the casting process, it is important to understand how these parameters affect meniscus behavior and slag consumption both qualitatively and quantitatively.

This paper presents a computational model of transient thermo-fluid flow of slag and steel in the meniscus region that can simulate the transient temperature distribution, fluid flow velocities, movement of the interface between the phases, formation of the solid and liquid slag layers, and slag consumption. The model is validated by experimental measurements of a caster simulator and applied in a parametric study of the effect of changing casting parameters on slag consumption.

II. LITERATURE REVIEW

To gain insight into the slag layers and phenomena in the meniscus region, computational models have evolved over many years. Early modelers[5,20,21] including Nakano *et al.*[5] analyzed slag melting as one-dimensional (1D) heat transfer in the slag layers above the molten steel. Thermal properties were varied with slag form (powdered, sintered, or molten) according to a packing factor, that was related to the sintering rate with a modified Jander's[22] equation. This model matched steady-state temperature measurements in the powder and the measured slag thickness, but, the liquid conductivity had to be increased four times (without oscillation) or six times (with oscillation) to account for the un-modeled convection in the liquid slag. This work shows the importance of temperature-dependent properties, mold oscillation, and convection effects on the slag heat transfer.

Many numerical and semi-analytical models have focused on fluid flow and heat transfer in the gap between the steel shell and mold wall.[10,23–28] Many of these assume constant slag viscosity.[23–26] Anzai *et al.*[23] modeled isothermal slag flow in the mold-strand gap as drag flow between two fixed non-parallel surfaces and found pressure increased with increasing slag viscosity, which matched measurements. This model predicts that slag consumption increases when the mold moves downward during each oscillation cycle and reverses when the mold moves upward. A similar model by Takeuchi and Brimacombe[10] included temperature dependent viscosity and found the same relation.

Several analytical models coupled lubrication theory with heat conduction to model solid, liquid slag layer thickness, and heat flux.[29–31] Bland[29] had temperature-dependent slag viscosity of the form $\mu(T) = A_1 e^{-A_2 T}$ where μ, T are viscosity and temperature, respectively, and A_1, A_2 are constants. The predicted slag consumption was in the lower end of plant observations. Bland's model was improved by Fowkes and Woods[30] by dividing the slag layer above and below the tip of the solidifying steel shell. Fowkes explained slag flow with a pumping mechanism with slag consumption occurring during the negative strip time, when the downward velocity of the mold wall exceeds the casting speed. Hill *et al.*[31] improved the Fowkes predicted solid and liquid slag thickness, OM shape and concluded that OM depth depends on slag viscosity, casting speed, and oscillation stroke. The predicted OM thickness in this study was similar to plant measurements[32,33] but slag consumption was not predicted. Steinruck and Rudischer[34] modeled OM formation by modeling slag flow, heat transfer, and solidification of strand shell simultaneously. Their model predicted that slag consumption (kg/m^2) decreases with casting speed with fixed stroke and matched experimental values reasonably well. However, they found the relation with consumption and oscillation frequency and stroke to be non-monotonic, but these predictions were not validated quantitatively.

Meng and Thomas[35] coupled a gap lubrication model of the interfacial gap with a 1D transient model of the solidifying steel shell and a 2D steady-state model of heat conduction in the mold. This software, named "CON1D," can accurately predict shell thickness, liquid/solid slag-layer thickness, slag, shell, and mold temperatures, heat flux, and other casting variables when calibrated correctly with plant measurements. Based on the input total slag consumption, the slag velocity model includes solid slag, liquid slag, and slag dragged downward in OMs. Heat transfer across the interfacial gap is modeled as radiation and conduction including the effects of air-gap formation, contact resistance, and liquid slag viscosity with temperature-dependent exponential function. This model has been used by many researchers for process analysis,[36–39] problem solving,[1,40,41] and control[42] of continuous casting, while others[39,43] have input CON1D results as initial conditions into advanced models to save computation. Details of CON1D are available elsewhere.[35,41,44]

Many researchers have measured slag consumption,[19,45–49] OM depth,[10,19,49] and hook depth,[50,51] as related to casting conditions and slag viscosity. Extensive plant measurements on a conventional slab caster at POSCO by Shin *et al*.[19] related slag consumption, OM and hook depth to casting speed, oscillation frequency, and slag properties such as surface tension, density, and viscosity. Total slag consumption was divided into three components—solid and liquid layer (lubrication) and OM consumption similar to CON1D formulation and with an empirical model to predict each part. The empirical equation, matches well with plant measurements, but requires a fitting constant to include the important effect of powder properties. It also matches the trends of casting condition effects on slag consumption of other studies.[46,49,52] This model of steady-state slag consumption is a useful tool to validate computational models. The measured trends are discussed in further detail later.

McDavid and Thomas[53] developed a 3D coupled heat-transfer and fluid-flow finite element model to analyze the top surface slag layers. This model used different temperature-dependent viscosity, thermal conductivity, and specific heat functions for regions of melting powder or solidifying liquid slag. The slag/steel interface shape and slag consumption were fixed to match plant measurements, and shear stress distribution along the interface was applied from a separate 3D model of molten steel flow. The predicted slag layer thickness profiles matched with plant measurements, and revealed a large flow recirculation in the liquid slag. Zhao *et al*.[54] confirmed this single long thin recirculation for most conditions, and also showed that many small natural convection cells can form, but only for very small steel surface velocities. Modeled steel and slag velocities diminish toward the meniscus around the mold perimeter, as flow of slag is due to consumption.[55,56]

Ojeda *et al*.[57,58] worked on a transient thermal-flow model of the meniscus region during an oscillation cycle, including the top slag layer, the slag rim, slag/steel interface, and the gap between the mold wall and the top ~70 mm of the steel shell. Temperature-dependent slag properties were used following McDavid and Thomas[53] The predicted flow behavior in the meniscus region during an oscillation cycle agreed well with works by Sengupta *et al*.[59] and the predicted slag consumption matched with plant measurements.[23] However, the fixed gap size needed by the model was not explained, and it has not been applied in parametric studies.

Recently, a complex model by Lopez *et al*.,[60,61] couples together heat transfer and flow in the molten steel and slag layers, mold wall, and solidifying steel shell. This 2D model of half of a caster extends ~1.5 m from top of the non-moving mold. Utilizing a very fine adaptive mesh, this model uses the VOF method[62] to track the slag/steel interface and the enthalpy-porosity technique[63] to model the steel solidification. The slag viscosity is temperature dependent, but the conductivity is constant, and the slag/mold interface oscillates. The predicted transient flow field agreed qualitatively with Ojeda *et al*.,[58] the heat flux behavior agreed qualitatively with Badri *et al*.[64,65] at 45 mm below the meniscus, and the trend of decreasing slag consumption with increasing casting speed agreed with Shin *et al*.[19] The flow rate of slag powder into the top of the domain was a fixed boundary condition, but the effect of this input condition on the ability of the model to predict slag consumption was not reported. Finally, the reported simulation time of 120 hours per case on a dual-core pc may limit its use for extensive parametric study.

Previous work has shed light on methods to model thermo-fluid behavior in the meniscus region and slag consumption. No model yet can accurately predict slag consumption for arbitrary plant conditions. The current work presents an efficient model of transient thermal-flow in the meniscus region during oscillation that is validated with both lab and plant measurements, and is applied in a parametric study to predict slag consumption.

III. COMPUTATIONAL MODEL DEVELOPMENT

A. *Governing Equations*

A two-dimensional two-phase (slag and steel) thermo-fluid model has been developed to predict transient fluid-flow and temperature in the region near the mold hot face and meniscus of a continuous slab caster, including the oscillating solid mold. A single set of momentum, continuity, and energy equations are solved on a fixed grid using the volume-of-fluid method (VOF) to determine the slag and steel phase regions in the fluid domain.

The two incompressible fluid phases are identified by a single phase fraction marker function, represented by the volume fraction of steel, α_{Fe}, which is advected by the flow according to the following conservation equation,

$$\frac{\partial \alpha_{\mathrm{Fe}}}{\partial t} + \boldsymbol{v} \cdot \nabla \alpha_{\mathrm{Fe}} = 0, \qquad [1]$$

where $\boldsymbol{v}$ is the vector of velocity components. The volume fraction of slag (α_{sl}) is calculated from total volume conservation:

$$\alpha_{\mathrm{Fe}} + \alpha_{\mathrm{sl}} = 1. \tag{2}$$

Material properties in each point in the domain are represented using mixture equations of α_{sl} and α_{Fe}, such as Eq. [3] for density of the fluid (ρ_{mix}).

$$\rho_{\mathrm{mix}} = \alpha_{\mathrm{Fe}}\rho_{\mathrm{Fe}} + (1 - \alpha_{\mathrm{Fe}})\rho_{\mathrm{sl}}, \tag{3}$$

where (ρ_{sl}) and (ρ_{Fe}) are constant densities of slag and steel. Continuity is satisfied by the following equation:

$$\frac{\partial \rho_{\mathrm{mix}}}{\partial t} + \nabla \cdot (\rho_{\mathrm{mix}}\boldsymbol{v}) = 0. \tag{4}$$

For momentum conservation, a single set of Navier–Stokes equations given by Eq. [5] is solved.

$$\rho_{\mathrm{mix}}\frac{\partial \boldsymbol{v}}{\partial t} + \rho_{\mathrm{mix}}\boldsymbol{v}\cdot\nabla\boldsymbol{v} = -\nabla p + \nabla\cdot\left[\mu_{\mathrm{mix}}\left(\nabla\boldsymbol{v} + \nabla^{T}\boldsymbol{v}\right)\right] + \rho_{\mathrm{mix}}\boldsymbol{g} + \boldsymbol{F}_{\sigma}, \tag{5}$$

where $\boldsymbol{F}_{\sigma}$ is the force source term due to surface tension given by the following equation, which is modeled using the CSF model of Brackbill *et al.*[66]

$$\boldsymbol{F}_{\sigma} = \sigma_{\mathrm{sl-Fe}}\frac{\rho_{\mathrm{mix}}\kappa\nabla\alpha_{\mathrm{sl}}}{\frac{1}{2}(\rho_{\mathrm{sl}} + \rho_{\mathrm{Fe}})}. \tag{6}$$

Here, $\sigma_{\text{sl-Fe}}$ is the constant surface tension of the interface between the slag and steel (N/m), and κ is the local curvature of this interface, found from

$$\kappa = \nabla\cdot\hat{\boldsymbol{n}}, \tag{7}$$

where $\hat{\boldsymbol{n}}$ is the unit normal ($\hat{\boldsymbol{n}} = \boldsymbol{n}/|\boldsymbol{n}|$) of the surface, found from the phase fraction marker field, $\boldsymbol{n} = \nabla\alpha_{\mathrm{sl}}$. At the wall boundary, $\hat{\boldsymbol{n}}$ is found from

$$\hat{\boldsymbol{n}} = \hat{\boldsymbol{n}}_{\mathrm{wall}}\cos\theta_{\mathrm{eq}} + \hat{\boldsymbol{n}}_{\mathrm{t}}\sin\theta_{\mathrm{eq}}, \tag{8}$$

where $\hat{\boldsymbol{n}}_{\mathrm{t}}$ is normal to the interface where it contacts the wall and $\hat{\boldsymbol{n}}_{\mathrm{wall}}$ is normal to the wall. The angle, θ_{eq}, is the static contact angle when the fluids are at rest. The angle may change (dynamic contact angle, θ_{d}) with interface motion. Without measurements to establish a constitutive law for θ_{d}, θ_{eq} is used in practice.[67]

Temperature in both the fluid (slag-steel) and solid (mold) regions of the domain is found by first solving the following enthalpy formulation of the energy equation.

$$\frac{\partial}{\partial t}(\rho_{\mathrm{mix}}h_{\mathrm{mix}}) + \nabla\cdot(\rho_{\mathrm{mix}}\boldsymbol{v}h_{\mathrm{mix}}) = \nabla\cdot(K_{\mathrm{eff}}\nabla T), \tag{9}$$

where temperature, T is found from the enthalpy of the mixture, h_{mix}, *via*

$$h_{\mathrm{mix}} = \int_{T_{\mathrm{ref}}}^{T} (c_{\mathrm{p}})_{\mathrm{mix}}\mathrm{d}T, \tag{10}$$

where c_{p} is specific heat, and T_{ref} is an arbitrary reference temperature. For the VOF model, h_{mix} is a mass average weighted over the phase fractions of the slag and steel,

$$h_{\mathrm{mix}} = \frac{(\alpha\rho h)_{\mathrm{sl}} + (\alpha\rho h)_{\mathrm{Fe}}}{(\alpha\rho)_{\mathrm{sl}} + (\alpha\rho)_{\mathrm{Fe}}}. \tag{11}$$

Thermal conductivity of the fluid, K_{eff} is the sum of the mixture conductivity (K_{mix}) and the conductivity due to turbulence (K_{t}). For turbulence closure, Menter *et al.*'s[68,69] k-ω SST model is used. Following the k-ω SST formulation, two more transport equations are solved for turbulent energy (k) and specific dissipation rate (ω),

$$\begin{aligned}
&\frac{\partial}{\partial t}(\rho_{\mathrm{mix}}k) + \nabla\cdot(\rho_{\mathrm{mix}}k\boldsymbol{v}) = \nabla\cdot[(\mu_{\mathrm{mix}} + \sigma_{\mathrm{k}}\mu_{\mathrm{t}})\nabla k] - \beta^{*}\rho_{\mathrm{mix}}\omega k + \tilde{P}_{\mathrm{k}}\\
&\frac{\partial}{\partial t}(\rho_{\mathrm{mix}}\omega) + \nabla\cdot(\rho_{\mathrm{mix}}\omega\boldsymbol{v}) = \nabla\cdot[(\mu_{\mathrm{mix}} + \sigma_{\omega}\mu_{\mathrm{t}})\nabla\omega] - \beta\rho_{\mathrm{mix}}\omega^{2} + \frac{\gamma}{v_{t}}\tilde{P}_{\mathrm{k}}\\
&\qquad + 2(1 - F_{1})\rho_{\mathrm{mix}}\sigma_{\omega 2}\frac{1}{\omega}\frac{\partial k}{\partial x_{\mathrm{j}}}\frac{\partial\omega}{\partial x_{\mathrm{j}}},
\end{aligned} \tag{12}$$

where the production term, $\tilde{P}_{\mathrm{k}}$, is

$$\tilde{P}_{\mathrm{k}} = \min\left[\mu_{\mathrm{t}}\frac{\partial v_{\mathrm{i}}}{\partial x_{\mathrm{j}}}\left(\frac{\partial v_{\mathrm{i}}}{\partial x_{\mathrm{j}}} + \frac{\partial v_{\mathrm{j}}}{\partial x_{\mathrm{i}}}\right); 10\beta^{*}\rho k\omega\right]. \tag{13}$$

The other terms are given by

$$F_{1} = \tanh\left(\left[\min\left\{\max\left(\frac{\sqrt{k}}{0.09\omega y}; \frac{500v}{y^{2}\omega}\right), \frac{4\rho_{\mathrm{mix}}\sigma_{\omega 2}k}{\mathrm{CD}_{k\omega}y^{2}}\right\}\right]^{4}\right), \tag{14}$$

where,

$$\mathrm{CD}_{\mathrm{k}\omega} = \max\left(2\rho_{\mathrm{mix}}\sigma_{\omega 2}\frac{1}{\omega}\frac{\partial k}{\partial x_{\mathrm{j}}}\frac{\partial\omega}{\partial x_{\mathrm{j}}}, 10^{-10}\right) \tag{15}$$

and

$$\begin{aligned}
&v_{\mathrm{t}} = \frac{\mu_{\mathrm{t}}}{\rho_{\mathrm{mix}}} = \frac{a_{1}k}{\max(a_{1}\omega;\, |\boldsymbol{S}|F_{2})};\\
&F_{2} = \tanh\left(\left\{\max\left(2\frac{\sqrt{k}}{0.09\omega y}; \frac{500v}{y^{2}\omega}\right)\right\}^{2}\right).
\end{aligned} \tag{16}$$

Here y is the distance to the closest wall node, $\boldsymbol{S}$ is strain rate tensor and the constants ϕ (β^{*}, β, σ_{k}, σ_{ω}, γ) are calculated based on Eq. [17].

$$\phi = F_{1}\phi_{1} + (1 - F_{1})\phi_{2}. \tag{17}$$

The constants are—$\sigma_{\mathrm{k}1} = 0.85$, $\sigma_{\mathrm{k}2} = 1.0$, $\sigma_{\omega 1} = 0.5$, $\sigma_{\omega 2} = 0.856$, $\beta_{1} = 0.075$, $\beta_{2} = 0.0828$, $a_{1} = 0.31$, $\beta^{*} = 0.09$, $\gamma_{1} = \frac{5}{9}$, and $\gamma_{2} = 0.44$.

F_{1} is the blending function and $F_{1} = 1$ in the near-wall region (activates $k - \omega$) and $F_{1} = 0$ in the outer region (activates $k - \epsilon$).

B. *Model Domains*

Figure 2 shows the two domains of this model: the fluid and the mold. The fluid domain contains powder, molten slag, and molten steel in the meniscus region extending 100 mm (width) from the mold wall and a length from 100 mm below to 50 mm above the tip of the solidifying steel shell (length). Flow in this small region is relatively unaffected by molten steel flow[53] and is mainly dominated by mold oscillation. The fluid domain also includes part of the interfacial gap between the steel shell and the mold wall, but it does not include the solidifying steel shell. The thickness profiles of the slag layer gap and the shape of the steel shell are predefined by the domain shape, based on output from CON1D[35] model simulations for the casting conditions of this problem. The input data for the CON1D simulations are included in Appendix Table A1. The OM shape, assumed to be triangular in CON1D, is simplified to constant thickness over the length of the steel strand, to carry the same slag consumption. In the fluid domain, the Navier–Stokes equations, turbulence, VOF, and energy equations are solved for the 2D velocity, pressure, and temperature fields.

The second domain is solid and contains the top of the copper mold adjacent to the fluid domain. The 3D geometry of the real mold plate is accurately modeled using a 2D rectangular mold plate with effective thickness, d_{eff}, without the water channels, by applying an effective convection boundary condition.

The mold domain is slightly longer than the fluid domain on both ends, to cover the range of movement of the mold mesh. Only the energy equation is solved in this domain for the 2D temperature field. The two domains are coupled by heat transfer across the vertically moving coincident surfaces that connect them.

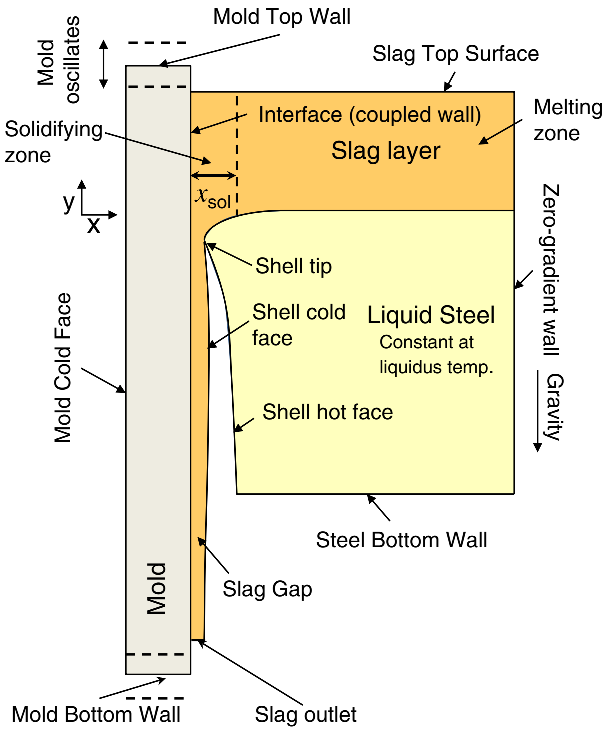

Fig. 2—Schematic of model domain and boundaries (not drawn to scale).

C. *Boundary Conditions*

1. *Slag top surface*

This "pressure inlet"[70] boundary is given a constant pressure, p_{i}, with velocity direction set to normal to the surface. The boundary temperature is set to a constant, T_{a}.

2. *Slag outlet*

This is another constant pressure boundary, where pressure is set to p_{o} (operating density[70] is ρ_{sl}) and velocity direction is normal to the surface. Heat flux across the boundary is set to zero. To avoid convergence problems, fluid entering the domain was given a "backflow" temperature of T_{b} that varied linearly from the mold hot face to the steel shell surface.

3. *Zero-gradient wall*

The vertical right side of the fluid domain is a zero-shear wall where normal (x-direction) velocities, tangential (y-direction) velocity gradients, and normal heat flux are all zero;

$$v_{\mathrm{x}} = 0; \quad \frac{\partial v_{\mathrm{y}}}{\partial x} = 0 \text{ and } K_{\mathrm{eff}} \frac{\partial T}{\partial x} = 0, \qquad [18]$$

This condition is termed as "symmetry wall".[70]

4. *Shell cold face*

The steel side of the gap is a vertical "no-slip" wall that moves downward at a constant velocity, the casting speed ($v_{\mathrm{x}} = 0$, $v_{\mathrm{y}} = v_{\mathrm{c}}$). It is given the fixed temperature profile ($T = T_{\mathrm{sc}}$) predicted by the CON1D simulation.

5. *Shell hot face*

The shell contacting the liquid steel is modeled as a constant temperature ($T = T_{\mathrm{sh}}$) stationary wall ($v_{\mathrm{x}} = 0$; $v_{\mathrm{y}} = 0$). The solidus temperature is used as T_{sh} and is calculated from the steel composition (Appendix—Table A2) using an analytical Clyne–Kurz style equation by Won and Thomas[71] in CON1D.

6. *Steel bottom surface*

This surface is modeled as a stationary wall ($v_{\mathrm{x}} = 0$; $v_{\mathrm{y}} = 0$) with zero heat flux ($q_{\mathrm{s}} = 0$).

7. *Mold cold face*

The mold surface that approximates the cooling channels is a convection boundary that removes heat to the cooling water:

$$q_{\mathrm{s}} = h_{\mathrm{c}}(T_{\mathrm{w}} - T_{\mathrm{s}}), \qquad [19]$$

where q_{s} is the cold-face heat flux, h_{c} is the effective convection heat-transfer coefficient, T_{w} is the average water temperature, and T_{s} is the local mold surface temperature. The effect of the water channel depth (d_{ch}), width (w_{ch}), and spacing (l_{ch}) is incorporated into h_{c} by treating the channels as heat-transfer fins using Eqs. [19] through [21] in CON1D.[35] The equations for h_c also include an empirical heat transfer coefficient from the water-channel sides and root to the water[72] and the thermal resistance of a scale layer (if present).

8. *Mold top and bottom wall*

The top and bottom surfaces of the mold are insulated surfaces ($q_s = 0$) because heat transfer from those surfaces is negligible[35] and heat flow is mainly perpendicular to the mold hot face.

9. *Mold domain velocity*

The entire solid (mold) domain is prescribed a velocity according to the mold oscillation:

$$v_x = 0;\ v_y = v_m = 2\pi a f\{1 - c\cos(2\pi f t)\}\cos\{2\pi f t - c\sin(2\pi f t)\}, \qquad [20]$$

where constant, $c = 4\pi\alpha_m/(8 - \pi^2\alpha_m^2)$, amplitude, $a = s/2$, s = stroke, f = frequency, and t = time. The modification ratio, $\alpha_m = 4A_o f$, where A_o is the time difference between peaks of the displacement curves for non-sinusoidal oscillation and sinusoidal oscillation, where $\alpha_m = 0$; $v_m = 2\pi a f\cos(2\pi f t)$.

10. *Interface (coupled wall)*

The interface between the fluid and mold domains is coupled in both velocity and heat flux. This interface moves with the mold velocity ($v_x = 0$; $v_y = v_m$) and has a no-slip condition on the fluid side. The instantaneous heat flux between points on the mold and fluid domain that are currently adjacent is same at every time. Details of this method is available elsewhere.[70]

11. *Fluid domain*

A reference pressure of 1 atm is set at a point 5 mm below the slag top surface of the domain and 2 mm away from the zero gradient wall. To maintain the continuous supply of energy provided by the liquid steel, the temperature of the steel phase ($\alpha_{Fe} \geq 0.98$) of the entire fluid domain is kept constant at T_{sh}, which represents a small superheat temperature difference above the liquidus. The values of the different variables used in the boundary conditions are given in Table I.

D. *Powder and Slag Properties*

The mold powder and slag properties vary greatly with composition and temperature, and evolve during the process. The composition differs from that reported by the supplier because the reported F content must be converted to CaF_2. In addition, the carbon added to slow the mold powder melting rate burns away completely during sintering, so is absent from the liquid slag.[73] Finally, the molten slag accumulates alumina inclusions from the steel, which changes its composition during operation.

The compositions of the commercial mold powder and slag in the current work, slag P2 in Shin *et al.*,[19] are given in Table II. Column 2 gives the reported composition[19,74] with components, X_{rep}. The reported F content is converted to CaF_2 (Eq. [21]), assuming that the required oxygen is provided by CaO according to the reaction: $2CaO + 4F \rightarrow 2CaF_2 + O_2$. This also requires a correction of CaO (Eq. [22]).

$$(CaF_2)_{corr} = \mathrm{pct}(F)_{rep} \times \frac{M_{CaF_2}}{2 \times M_F}, \qquad [21]$$

$$(CaO)_{corr} = \mathrm{pct}(CaO)_{rep} - \mathrm{pct}(F)_{rep} \times \frac{M_{CaO}}{2 \times M_F}, \qquad [22]$$

where the molecular weights are, $M_{CaF_2} = 78.07$, $M_{CaO} = 56.08$, $M_F = 19$. To calculate the mold powder composition, X_p, the reported wt pct of each component in the powder, pctE_i, including every oxide, $(CaF_2)_{corr}$, $(CaO)_{corr}$, and C-Total, is multiplied by the factor, F_p (Eq. [23]) and is shown in column 3 of Table II.

$$F_p = \frac{100}{\sum \mathrm{pct}E_i - \sum \mathrm{pct}C_i}, \qquad [23]$$

where pctC_i = wt pct of C-Free and CO_2.

To calculate the initial molten slag composition, X_{lo}, the carbon is reduced to zero, and Eq. [23] is applied to column 2 with pctC_i = C-Total, C-Free and CO_2 to give column 4, Table II.

During operation, some of the alumina inclusions in the molten steel are "picked up" and absorbed into the liquid slag layer, which changes the slag composition and properties with time during operation. To calculate the molten slag composition during operation, (X_l), the wt pct of all elements (X_{lo}) except alumina is multiplied by a factor, $F_{Al_2O_3}$ given by Eq. [24].

$$F_{Al_2O_3} = \frac{100}{\sum G_i + \mathrm{pct}(Al_2O_3)_{pickup}}, \qquad [24]$$

where pctG_i = wt pct of all slag components including Al_2O_3. The increased wt pct of Al_2O_3 can be calculated by multiplying $F_{Al_2O_3}$ by the sum of the initial alumina in the slag and the alumina pickup. The final slag composition during operation is given in column 5, Table II for slag P2 assuming ~7 pct Al_2O_3 pickup.

1. *Slag Viscosity*

Several models have been developed to estimate molten slag viscosity based on its composition and temperature during cooling, based mainly on Arrhenius or Weymann relations.[75–78] A widely used model, by Riboud *et al.*[75] based on 45 slags, gives slag viscosity as

$$\mu = AT\exp\left(\frac{B}{T}\right), \qquad [25]$$

where T is temperature in Kelvin and A, B are parameters defined as follows

$$\ln A = -19.81 + 1.73\left(X_{CaO} + X_{MnO} + X_{MgO} + X_{FeO} + X_{B_2O_3}\right) + 5.82X_{CaF_2} + 7.02\left(X_{Na_2O} + X_{K_2O} + X_{Li_2O}\right) - 35.76X_{Al_2O_3}, \qquad [26]$$

Table I. Variables Used in Model

Variable	Shin Case	Badri Case
Mold geometry		
d_{ch}	20 mm	13.65 mm
w_{ch}	5 mm	7.9 mm
l_{ch}	19 mm	15.8 mm
d_{eff}	20 mm	8.58 mm
Boundary conditions		
p_i	1 atm	1 atm
p_0	1 atm	1 atm
h_c	45,272 W/m^2 K	16,720 W/m^2 K
T_a, T_w	313 K (40 °C)	310.85 K (37.85 °C)
T_r	300 K (27 °C)	310 K (37 °C)
T_b	496 K to 1635 K (223 °C to 1362 °C)	1400 K (1127 °C)
T_{sc}	$f(y)$, 1805.9 K to 1634.72 K (1532.9 °C to 1361.72 °C)	1791.7 K (1518.7 °C)
T_{sh}	1805.9 K (1532.9 °C)	1804.87 K (1531.87 °C)
Casting conditions		
v_c	0.02323 m/s (1.39 m/min)	0.0127 m/s (0.762 m/min)
s	5.89 mm	6.3 mm
f	2.9 Hz	1.3 Hz
α_m	0	0

Table II. Mold Slag Composition

Components	Reported by Suppliers, X_{rep} (wt pct)	Powder Composition, X_p (wt pct)	Initial Molten Slag Composition, X_{lo} (wt pct)	Final Molten Slag Composition, X_l (wt pct) (~7 pct Al_2O_3 pickup)
SiO_2	37.77	39.48	40.58	37.94
CaO	37.88	28.42	29.21	27.32
MgO	1.98	2.07	2.13	1.99
Al_2O_3	4.99	5.22	5.36	11.50
TiO_2	0.03	0.03	0.03	0.03
Fe_2O_3	0.31	0.32	0.33	0.31
MnO_2	0.04	0.04	0.04	0.04
P_2O_5	0.01	0.01	0.01	0.01
Na_2O	3.75	3.92	4.03	3.77
K_2O	0.11	0.11	0.12	0.11
F	7.22	—	—	—
CaF_2	—	15.47	15.90	14.87
B_2O_3	1.2	1.25	1.29	1.21
Li_2O	0.9	0.94	0.97	0.90
C-total	2.59	2.71	—	—
C-free	1.62	—	—	—
CO_2	3.24	—	—	—

$$\begin{aligned} B = 31,140 - 23,896\big(X_{CaO} + X_{MnO} + X_{MgO} \\ + X_{FeO} + X_{B_2O_3}\big) - 46,356X_{CaF_2} \\ - 39,519(X_{Na_2O} + X_{K_2O} + X_{Li_2O}) + 68,833X_{Al_2O_3}. \end{aligned} \quad [27]$$

Here, X_i is the molar fraction of the ith compound.

Alumina content in the molten slag can increase as much as 30 pct[54] during casting. The temperature-dependent viscosity of the Shin-P2 molten slag, based on 2.31, 5.15, and 6.94 pct Al_2O_3 pickup are calculated using the Riboud model and compared in Figure 3 along with the measured viscosity by Shin *et al.*[19] The results show that the viscosity increases with increasing alumina pick-up, which agrees with the observations of many previous experimental studies.[79,80] Considering a typical fraction of alumina inclusions absorbed from the steel into this slag, a ~7 pct pick-up is assumed for the current model simulations of the commercial process.

A limitation of the Riboud model is that it does not predict the abrupt increase in viscosity observed at some temperature during cooling,[79] termed as the break temperature (T_{Br}). The following power-law relation[35] captures this phenomenon

$$\mu = \mu_o \left(\frac{T_o - T_{fsol}}{T - T_{fsol}} \right)^n, \quad [28]$$

where T_{fsol} and n are chosen empirically to fit measured data and μ_o is the viscosity measured at the reference temperature, T_o chosen to be 1573 K (1300 °C). Here, Eq. [28] was used with n and μ_o of 1.8 and 0.55 Pa s, respectively, selected for CON1D simulations to match the Riboud model near 1806 K to 1473 K (1533 °C to 1200 °C). To avoid numerical difficulties in the current model with very high viscosity at lower temperatures, the viscosity below 900 K (627 °C), was truncated to a constant (10^5 Pa s). The result is shown in Figure 4 for the Shin-P2 slag with 6.94 pct Al_2O_3 pick-up. This curve to model viscosity of the molten slag during cooling and solidification or crystallization was applied near the mold wall, as shown in the solidification zone in Figure 2, which has width x_{sol}, and includes the region above the slag rim.

In the top of the domain, where the mold powder sinters and melts, a different model was needed to characterize the slag viscosity. According to a previous review[81] and the previous model of powder viscosity by McDavid[12], as temperature increases, the mold powder viscosity increases as it sinters to form a semi-solid which has more resistance to flow than the powder. As it melts more fully, this resistance decreases, so the viscosity decreases again. These phenomena are taken into account in the viscosity model for heating, sintering, and melting powder, shown in Figure 4.

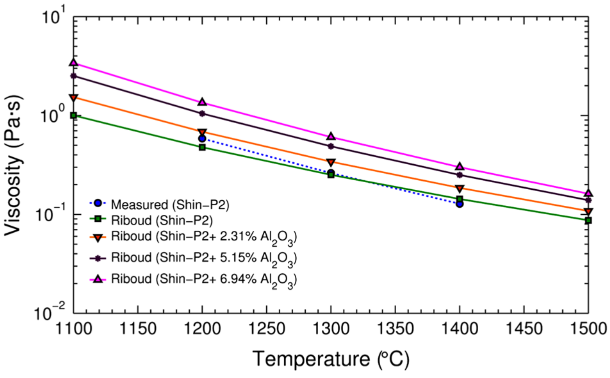

Fig. 3—Temperature dependent slag viscosity predicted by Riboud model for different pctAl_2O_3 pickup *vs* measured values.

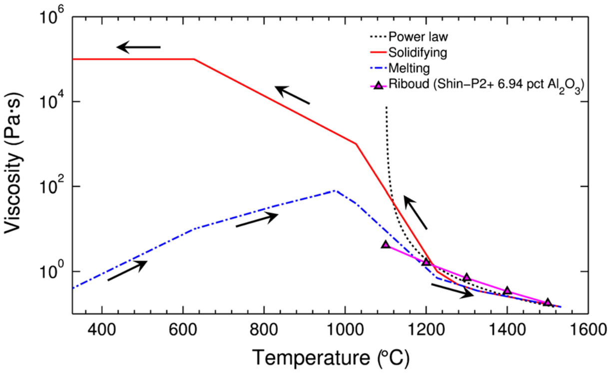

Fig. 4—Temperature dependent slag viscosity model during solidification and melting.

2. *Slag Thermal Conductivity*

Two different effective slag thermal conductivities are used during heating and cooling, as shown in Figure 5. The powder contains air which gives the mixture a low conductivity, ~0.3 W/m K.[82] As the powder heats, sinters, coalesces,[5] and melts, the air disappears[83] so its thermal conductivity gradually increases. Above the melting temperature, a constant effective thermal conductivity (3 W/m K) is used in the current model of slag P2. This assumes that the decrease in phonon conductivity with increasing temperature is balanced by the increase in radiation,[84] which agrees with the model of McDavid and Thomas[53] and the measurement of constant conductivity in molten slag systems of Hasegawa *et al.*[85] During cooling below the solidification temperature, Kishimoto's[86] conduction measurements for solid slag similar to P2 are adopted, which show decreasing conductivity with decreasing temperature. The thermal conductivity of the Badri slag has similar trends, but was assumed to have lower conductivity, due to the increased oxidation, gas bubbles, and crystal defects, that likely accompany the less-well-controlled lab experiment.

3. *Slag Specific Heat and Density*

The specific heat of slag in the current model is given in Figure 6. Measurements by Mills *et al.*[11] show a sharp increase in effective c_p at the glass transition temperature, T_g, due to the enthalpy of transition (ΔH) between liquid slag and solid. Density of the slag is fixed at 2500 kg/m^3.[19]

E. *Other Material Properties*

The surface tension of the interface between the molten steel and slag, $\gamma_{Fe(l)\text{-}sl}$, was calculated using Girifalco and Good's approach.[87]

$$\gamma_{Fe(l)-sl} = \gamma_{Fe(l)-gas} + \gamma_{sl-gas} - 2\Phi(\gamma_{Fe(l)-gas} \times \gamma_{sl-gas})^{0.5}, \quad [29]$$

where Φ represents attraction between the phases and for $CaO\text{-}Al_2O_3\text{-}SiO_2$ ternary system is given by;[87]

$$\Phi = 0.003731 \times (\text{pct}\,Al_2O_3) + 0.005973 \times (\text{pct}\,SiO_2) + 0.005806 \times (\text{pct}\,CaO). \quad [30]$$

For the final molten slag composition in Table II column 5, Φ from Eq. [30] is 0.4281. Extensive measurements of steel surface tension ($\gamma_{Fe(l)\text{-}gas}$)[87–91] show the importance of sulfur content. For ~0.011 pctS, $\gamma_{Fe(l)\text{-}gas}$ is 1.6 N/m in Ar gas. Surface tension ($\gamma_{sl\text{-}gas}$) of the (Shin-P2) commercial slag was supplied[19,74] as 0.419 N/m. From Eq. [29], the surface tension between liquid slag and steel is calculated to be 1.3 N/m.

Finally, the static contact angle (θ_{eq}) between liquid steel and liquid slag on solid steel was determined to be 160 deg, based on the work by Ojeda *et al.*[58], using Young's equation[92] for this three phase system.

During casting, sometimes air gaps form between the mold hot face and solid slag layer. The thermal

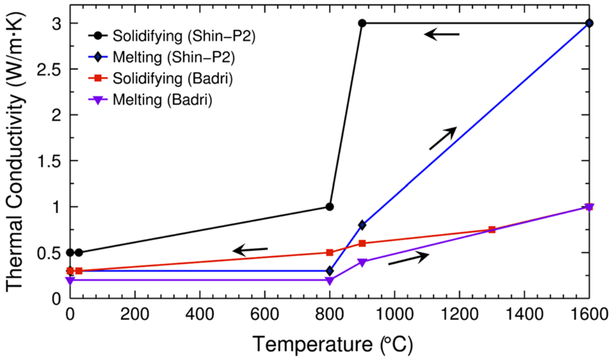

Fig. 5—Temperature dependent thermal conductivity model for slag melting and solidifying.

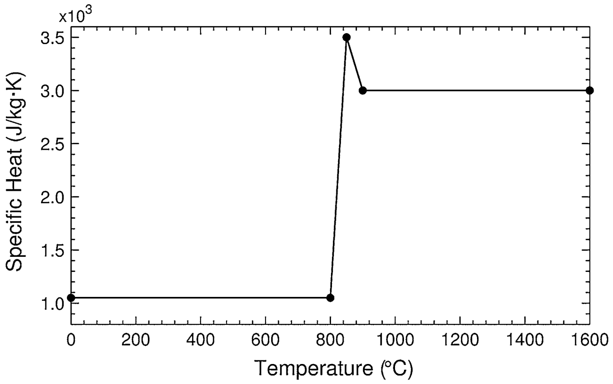

Fig. 6—Temperature dependent specific heat of slag.

Table III. Properties of Liquid Steel and Cu (Mold)

Properties\Material	Steel	Cu (Mold)	Unit
Density	7000	8900	kg/m^3
Thermal conductivity	30	350	W/m K
Specific heat	700	385	J/kg K
Viscosity	0.0063	—	Pa s

conductivity of the air in this air gap is significantly different than natural air. The presence of H_2 in the trapped air causes the thermal conductivity to vary greatly based on volume percentage of H_2. Nakato and Muchi[93] showed that conductivity of nitrogen-hydrogen mixture can vary from 0.03 to 0.17 W/m K. In current model the conductivity of air gap is taken as 0.06 W/m K. The liquid steel and copper (mold) properties are constant, given in Table III.

F. *Solution Procedure*

The coupled transient energy equation and incompressible Navier–Stokes equations are discretized using the finite volume method (FVM) and solved on a fixed, structured grid with quadrilateral elements for temperature, pressure, and velocity field using ANSYS FLUENT 13.0. While velocities and turbulence quantities are saved in cell-centers, pressure is computed in the face center using PRESTO scheme which mimics the staggered arrangement. Spatial discretization used second order upwinding for advection terms and a second-order central difference scheme with a least-squares gradient method for the diffusion terms. First-order implicit scheme is used for transient solution. A pressure-based segregated algorithm, pressure-implicit with splitting of operators (PISO), is used for coupling pressure and velocity. The VOF equation is solved using explicit time discretization and a geometric reconstruction scheme for face fluxes in cells where the interface is located.

This coupled transient thermal-flow problem is solved in several steps. First, the CON1D model is run to estimate the size of the interfacial gap, shape of the solidified steel shell, temperature profile of the mold cold face, air-gap thickness, cooling water temperature, and convection heat transfer coefficient. The solution starts with an initial guess of the phase fraction field, based on for the slag/steel interface shape calculated with Bikerman's equation,[94]

$$x = x_o - \sqrt{2b^2 - y^2} + \frac{b}{\sqrt{2}} \ln \frac{b\sqrt{2} + \sqrt{2b^2 - y^2}}{y}, \quad [31]$$

where,

$$x_o = b - \frac{b}{\sqrt{2}} \ln\left(\sqrt{2} + 1\right) \text{ and } b^2 = \frac{2\gamma_{\mathrm{Fe(l)-sl}}}{g(\rho_{\mathrm{Fe}} - \rho_{\mathrm{sl}})}. \quad [32]$$

Here, x is horizontal distance from the wall where the phases meet, y is vertical distance from the free surface. Then, the guess is improved by solving the isothermal flow equations including the VOF model, Eqs. [1] through [8], until steady-state is reached, assuming constant slag viscosity (0.1 Pa s) and no mold or shell movement. Next, the initial temperature field is obtained by solving the steady-state energy equation system, Eqs. [9] through [11], based on the phase fraction field with no flow. Finally, the complete transient coupled system of thermal-flow equations are solved (Eqs. [1] through [17]), with the mold domain moving according to the oscillation equation and the cold face of the steel shell moving downward at the casting speed. The solution is considered converged when results over successive oscillation cycles are the same, which usually takes only a few cycles.

For the Shin case, with a fixed time step of 10^{-5} seconds and fine mesh (1,76,450 cells with 0.1 × 0.1 mm cells near the interface and mold hot face) the ~0.4 seconds simulation takes 24 hours of computation on an Intel® Xeon® CPU with 6 × 2.6 GHz cores PC. The Badri case needed only 99,064 cells, for the same 0.1 × 0.1 mm refinement. The parametric study cases used a simplified domain with coarser mesh (5340 cells) after mesh independence studies showed reasonable accuracy, which required only 2.5 hours per 1 seconds run. In all cases, cells are smaller where the interface is expected to be located and in the gap where high temperature gradients and rapid changes in properties are expected.

IV. VALIDATION CASES

The model is validated by simulating two cases where different experimental and plant measurements were available. First, a typical commercial parallel-walled slab caster is simulated, and the predicted slag consumption is compared with plant measurements by Shin *et al.*[19] to validate the flow field. Second, a steel continuous casting simulator by Badri *et al.*[64,65] is modeled, and the predicted temperatures in the mold wall are compared with thermocouple measurements in this experimental apparatus to validate the heat transfer model.

A. *Commercial Caster (Shin) Case*

For simulating the commercial caster, where extensive, accurate slag consumption measurements were available, the casting conditions, mold geometry, and material properties described by Sengupta *et al.*[59] and Shin *et al.*[19] are used. The effective mold thickness is 20 mm for this commercial slab casting mold, with its 40-mm-thick mold plates and 20 mm deep water channels. The composition for slag P2 is given in Table II column 5 for an assumed ~7 pct Al_2O_3 pickup and its temperature-dependent properties are given in Figures 4 through 6. Casting conditions and steel properties for this case are given in Tables I and III, respectively. From the shell tip to the fluid domain bottom (100 mm below), the slag gap thickness increases from 0.665 to 0.981 mm thick and the shell thickness increases from 0 to 4.13 mm. There is no air gap for this case. Further conditions needed as input to CON1D to determine the shell thickness, gap size, and thermal parameters for this typical commercial casting conditions are given in Appendix Table A1. The start time of the final thermal-flow stage in Fluent is 0.77 seconds (2.25 cycles) before $t = 0$ where converged results are presented for one oscillation cycle.

B. *Experimental Simulator (Badri) Case*

Badri *et al.*[65] measured temperatures in a steel continuous-casting mold simulator with six pairs of thermocouples located 1.5 mm (termed "Hot") and 5 mm (termed "Cold") from the hot face of the mold, as shown in Figure 7. The effective mold thickness is 8.58 mm for the dimensions of this mold plate and its slots, which are shown in Figure 7. The current model predictions for this experiment are compared with the 12 temperature histories measured during the experiment and reported in Figure 176 in Badri[96] for Trial 32. Further experimental details are given by Badri *et al.*[64,65]

The 100 mm long slag gap for this case decreases in thickness from 0.9 to 0.04 mm from shell tip to 12 mm below it, then increases to 0.427 at domain exit. The shell thickness increases from 0 to 2.5 mm from shell tip to domain exit. The contact resistance and drop in heat transfer due to cracks and bubble formation during crystallization of the cooling slag is modeled as an air gap between the mold and slag layer. This air-gap thickness increases from 0.05 to 0.21 mm at the meniscus to the bottom of the fluid domain. Further conditions input to CON1D to determine the shell thickness, gap size, and thermal parameters for this case are given in Appendix Table A1. Converged results are presented for the fifth oscillation cycle.

C. *Flow Field Results*

The flow field in the meniscus region during one oscillation cycle is dominated by the oscillating mold along with the solid slag rim and their effect on interface between liquid slag and steel. The Badri and Shin case show similar flow behavior.

Taking the Shin case as an example, Figure 8 shows the displacement, velocity of the mold, and casting speed during one oscillation cycle. The time when the mold moves downward faster than the casting speed is termed negative strip time (NST, t_n). The rest of the period is called positive strip time (PST, t_p).

The velocity field variations and changing shape of the slag/steel interfacial meniscus ($\alpha_{Fe} = 0.5$) for the third oscillation cycle are shown in Figures 9(a) through (f). Starting from zero displacement with the mold moving upward at maximum velocity, Figure 9(a) shows that the rising slag rim pulls the meniscus upwards. This meniscus bulging lags behind the slag rim and has less movement. This causes the gap between the slag rim and the meniscus (region 1) to expand. Some of this slag is drawn upward into region 1 from the gap between the mold and steel shell (region 2).

After passing its highest position, the downward-moving slag rim starts to squeeze region 1, as shown in Figures 9(b) and (c). Combined with drag from the downward-moving mold, slag starts to enter region 2 to be consumed into the gap, just before the start of NST at 0.11 seconds. Figure 9(c) at 0.14 seconds shows slag being pushed out of region 1 both far away (right), and down into region 2. This flow increases as the mold reaches its maximum downward velocity at ~0.17 seconds (Figure 9(d)). The increasing pressure can be seen in Figure 10 at a typical point in the slag near the gap. The maximum pressure is reached just after NST at 0.258 seconds, when the mold is at its lowest position with zero velocity (Figure 8). At this time, the slag rim is pushed closest to the meniscus and region 1 is smallest. As the mold moves upward again, the slag "pumping" decreases and at 0.26 seconds (between Figures 9(e) and (f)) the flow direction reverses again.

This sequence of flow variations is repeated for every oscillation cycle. This mechanism is consistent with that proposed in previous work.[57,59] The movement of the three-phase contact line (point in this 2D model) between the steel/slag interface and the wall matches closely with the mold wall oscillation. This agrees exactly with previous observations in lab experiments using mercury or water with silicon oil.[6,7]

D. *Slag Consumption Results*

The current model predicts the transient behavior of slag consumption during an oscillation cycle. Both cases show similar behavior which is explained here using the Shin case in Figure 11. The negative sign means slag is flowing downward (positive consumption). The oscillating slag consumption curve (Figure 11) closely follows the oscillating mold velocity, which agrees with Anzai *et al.*[23] Slag consumption is positive only from 0.0846 to 0.2621 seconds, which overlaps NST. Slag is drawn upwards during the rest of the cycle. The result is an average consumption of 0.0051 kg/m s or 0.220 kg/m^2. From Shin *et al.*,[19] the measured consumption calcu-

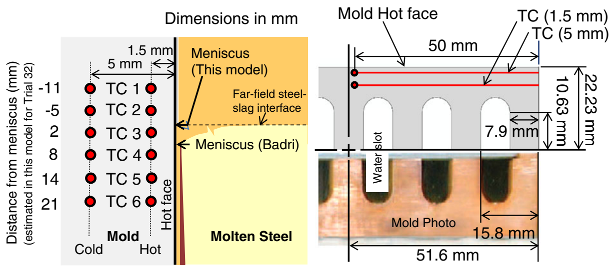

Fig. 7—Badri experiment thermocouple locations (left) and mold dimensions (right).

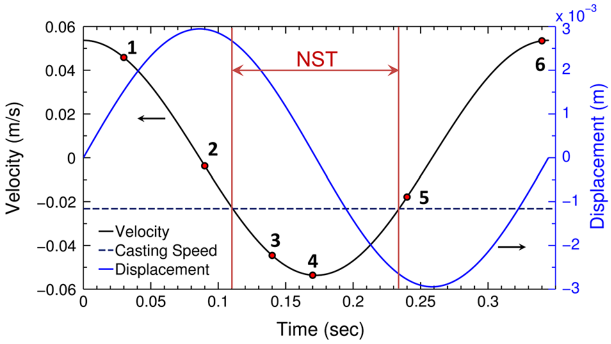

Fig. 8—Displacement, velocity, and NST time over one oscillation cycle (0.77 to 1.12 s) for Shin case.

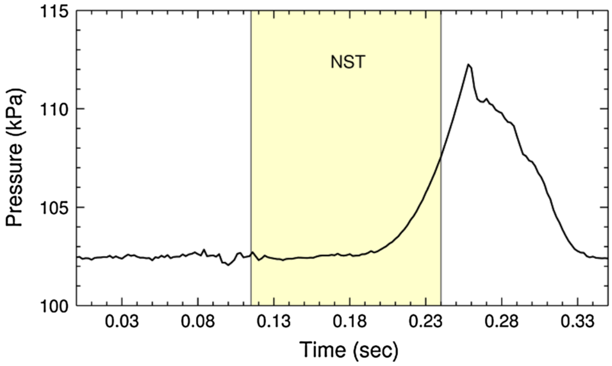

Fig. 10—Predicted slag pressure at 0.4 mm from hot face and 0.5 mm above shell tip (Shin case: 0.77 to 1.12 s).

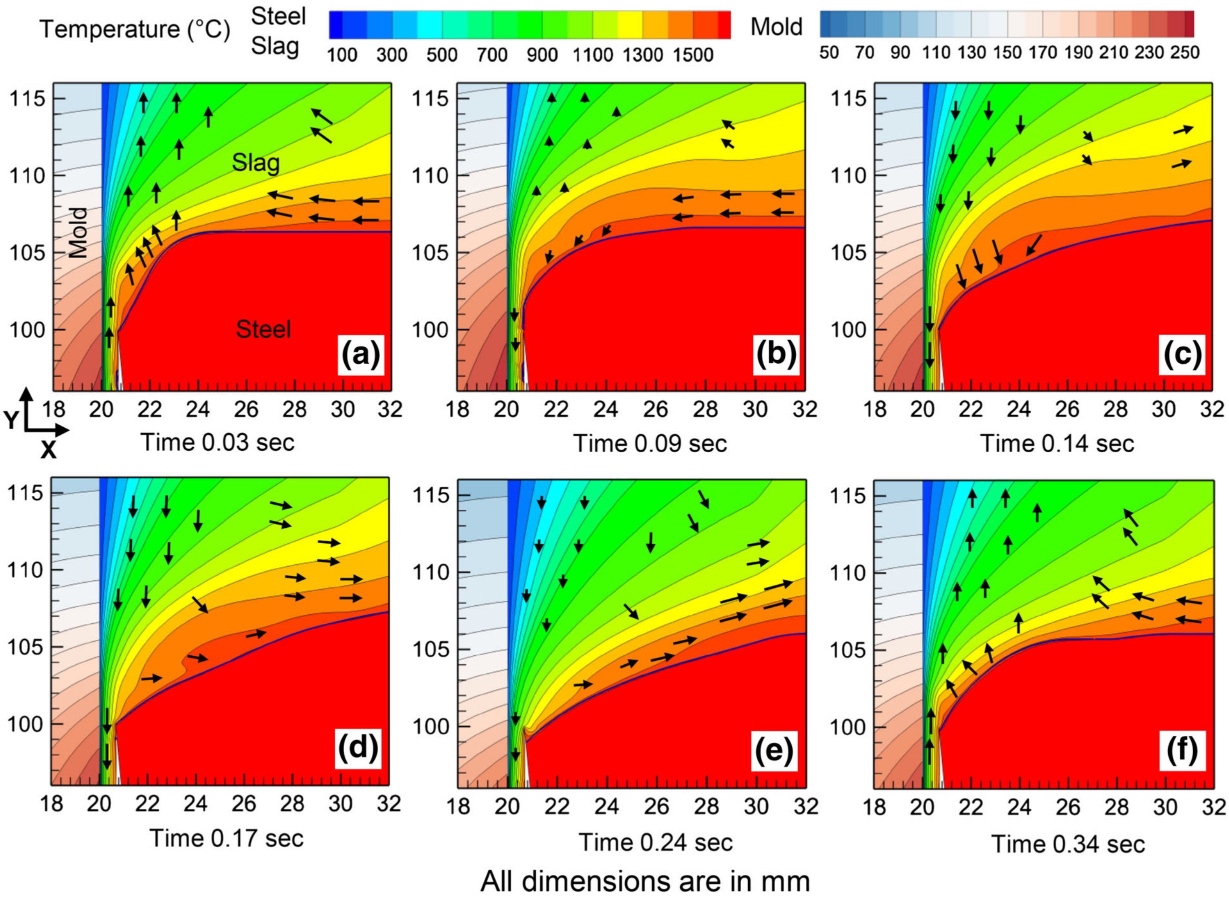

Fig. 9—Meniscus region events over one oscillation cycle (0.77 to 1.12 s) for Shin case.

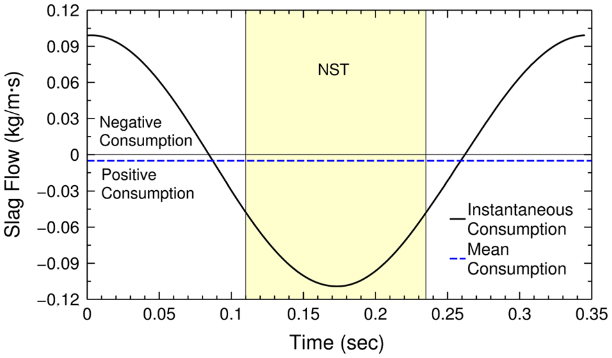

Fig. 11—Predicted instantaneous and mean slag consumption for Shin case (0.77 to 1.12 s).

lated for this slag, assumed to include alumina pickup (k_c = 14), and casting conditions is 0.236 kg/m^2. This agrees with the prediction within 8 pct. The disagreement might be due to treating the OMs as effective thickness[35] over the whole gap. Slag properties might be another source of error, as viscosity affects the slag consumption greatly.[46] Taking the errors into account, the model predictions of slag consumption agree well with measurements.

Consumption is found by integrating the velocity profile across the gap. Figure 12 shows the liquid and solid slag thickness across the gap grows slightly with distance down the mold, but varies very little during an oscillation cycle. Figure 13 shows the slag velocity profile across the gap, which oscillates with the mold over most of the gap, owing to the high viscosity of the solid slag near the wall. Slag is only consumed due to velocity variations in the thin liquid layer near the shell. Velocity profiles at different distances down the mold are nearly the same, except near the domain outlet due to the thermal backflow boundary condition. These results suggest that consumption is controlled more by drag inside the gap than by pressure at the meniscus.

Increasing gap size was found to increase consumption somewhat. Gap size is determined by the CON1D model, based on the casting conditions and calibration with measurements. Consumption for the Badri case is much larger (1.23 kg/m^2) than the Shin case, owing to the increased gap size, which is due to the decrease in casting speed and increase of stroke.

E. *Temperature Results*

Transient temperature predictions are shown in Figure 14 at the six hot thermocouples locations for the Badri case. Here the locations are fixed in space in the laboratory ("Eulerian") reference frame so do not oscillate with the mold. Predictions for each oscillation cycle are similar, indicating that the model has reached its intended pseudo-steady state. The temperatures measured by the six pairs of thermocouples by Badri[96] are shown in Figure 15. Because the thermocouples oscillate with the mold in a moving ("Lagrangian") reference frame, they are not expected to match with Figure 14. Time averaged temperatures calculated and measured over six oscillation cycles are compared in Figure 16 and a reasonable match is observed. Maximum temperature is found near the meniscus (TC4), especially in the measurements, and decreases more above the meniscus.

Figure 17 was constructed to predict the thermocouple results at TC3, TC4, and TC5 locations during a representative (fifth) oscillation cycle, by oscillating the reporting locations appropriately with time. The corresponding mold velocity and displacement curves are shown in Figure 18. Figure 17 also includes the measured transient temperatures over six different cycles by Badri *et al.*[65]

To extract the measured temperatures into Figure 17 required making some uncertain decisions. The far-field steel/slag interface at the top free surface was taken as the "meniscus" location, reported by Badri to specify the vertical locations of the thermocouples, and is 4.5 mm above the shell tip. Time starts at the beginning of the 0.258 seconds NST (marked with an arrow in the shaded region) for the reported oscillation period of 0.77 seconds for this case.[65] This was done for easy comparison with 0.175 seconds NST (0.83 seconds period) found in Figure 273 of Badri[96] for this same case. Offsetting the time axis to properly align the heat flux and temperature curves was difficult.

In Figure 17 the measurements show great variations between oscillation cycles, which are not modeled. However, the average temperature variations over a single cycle match reasonably well. As expected, thermocouples closer to the meniscus show larger temperature variations during each cycle, which are also summarized in Figure 16. This is due to greater variations in heat flux. For example, the maximum amplitudes, which are predicted at TC4 of 1.37 K (1.37 °C, cold) and 3.22 K (3.22 °C, hot) compare well with the measured amplitudes of 1.35 K and 3.04 K (1.35 °C and 3.04 °C). The amplitudes further below the meniscus, such as at TC5, are all clearly smaller.

During a single oscillation cycle, the predicted temperature increases to a maximum sometime during the NST, and then falls. This is consistent with many of the measurements, which show a mixture of trends. For example, at TC4, the measured temperature increases during NST for three of the cycles but decreases during the other three. Measured temperatures from similar experiments with ultra-low carbon steel by Badri (Trial 30, 31, and 35; Badri[96]) show other trends. Figure 19 shows that temperature for TC3 in Trial 31[96] consistently increases during NST.

F. *Phase Lag Results*

Temperature measurements in transient conditions always experience phase lag,[97,98] which increases with distance of the thermocouple from the surface where the varying heat flux is applied. Temperature, $T(x, t)$, near a surface subjected to a spatially constant heat flux that oscillates in time as $q = q_o \cos \omega t$ is given by the following semi-infinite solution.[97]

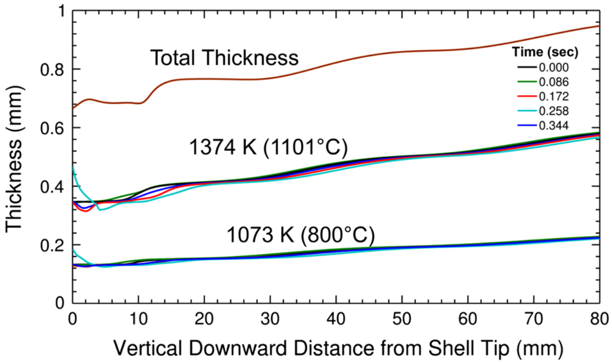

Fig. 12—Liquid slag thickness predicted by model based on 1374 K and 1073 K (1101 °C and 800 °C) constant temperature lines (Shin case: 0.77 to 1.12 s).

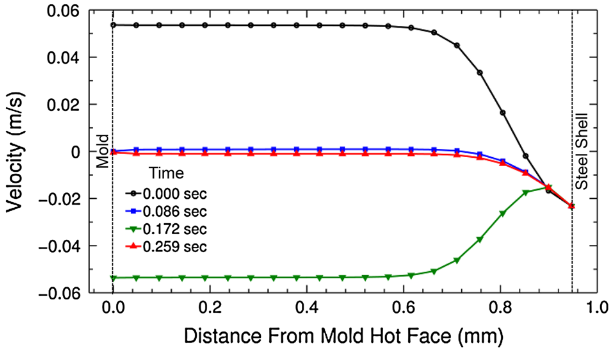

Fig. 13—Transient velocity in the slag gap (Shin case: 0.77 to 1.12 s).

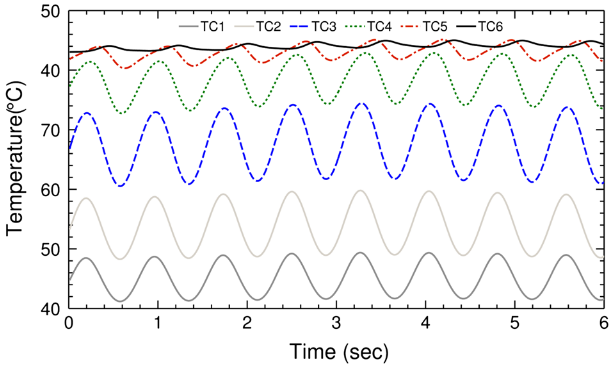

Fig. 14—Temperature predictions at TC (hot) locations over simulation time (Badri case: fixed in lab frame of reference).

$$T = T_{\mathrm{o}} + \frac{q_{\mathrm{o}}}{K}\left(\frac{\alpha_{\mathrm{T}}}{2\pi f}\right)^{0.5}\exp\left[-x\left(\frac{\pi f}{\alpha_{\mathrm{T}}}\right)^{0.5}\right]\cos\left[2\pi f t - x\left(\frac{\pi f}{\alpha_{\mathrm{T}}}\right)^{0.5} - \frac{\pi}{4}\right], \qquad [33]$$

where $\alpha_{\mathrm{T}} = K/\rho c_{\mathrm{p}}$. The surface temperature ($x = 0$) lags by $\frac{\pi}{4}$ or 12.5 pct of the oscillation period. Thermocouple measurements, and their model predictions, should show longer phase lags, increasing with distance from the surface. For the 1.3 Hz (0.769 seconds period) of the Badri case, the surface, hot, and cold thermocouples should experience lags relative to the heat flux of 0.098, 0.133, and 0.219 seconds, respectively. For the 2.9 Hz (0.345 seconds period) of the Shin case, these same three lags are 0.043, 0.068, and 0.126 seconds.

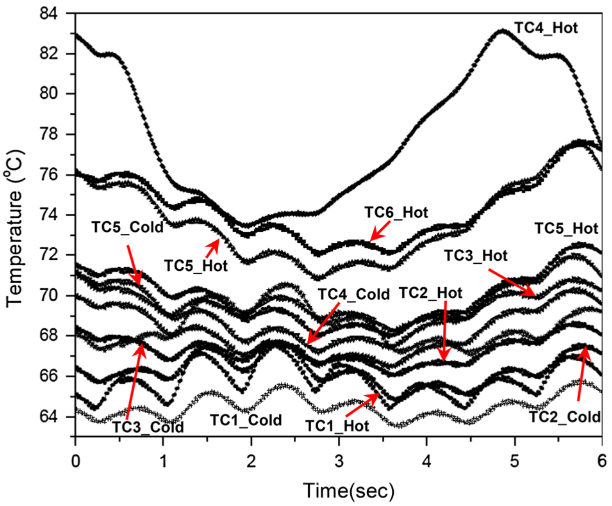

Fig. 15—Measured temperatures in Trial 32 reported by Badri.[96]

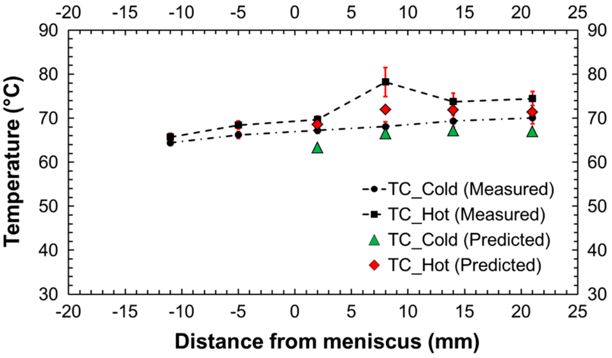

Fig. 16—Model averaged thermocouple predictions *vs* measured values by Badri averaged over six oscillation cycles (error bars indicate the range).

Although the meniscus region is a highly 2D heat flux region, it is useful to compare the current model results with the theoretical phase lags from the 1D equation. The current model of the Badri case predicts phase lags averaged over the six oscillation cycles of 0.038, 0.058, and 0.095 seconds for the surface, hot, and cold thermocouples at TC3, respectively. For the Shin case, the predicted phase lags average 0.025, 0.046 seconds for the hot and cold TC3, respectively.

Although these time lags are shorter than the 1D solution, they show the expected trends for both cases. Specifically, time lags increase with distance from the hot face surface and decrease with increasing frequency from the Badri case to the Shin case. The lower magnitude in the model is likely due to the 2D heat flux experienced in the meniscus region.

From Badri's raw temperature measurements (Figure 15) the lags between the thermocouple measure-

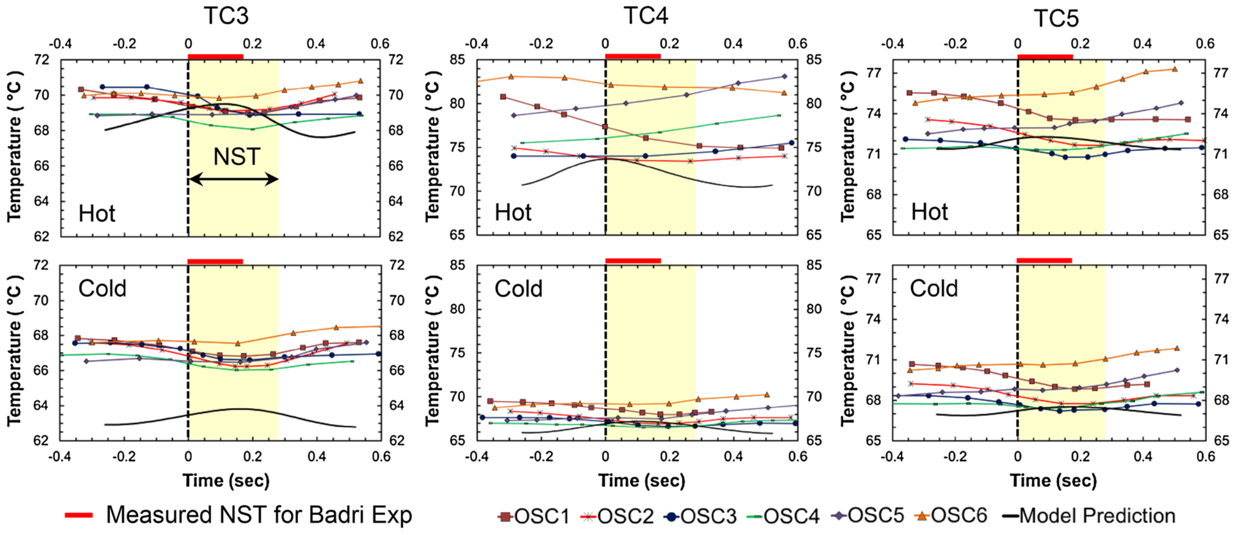

Fig. 17—Thermocouple prediction by model *vs* measured temperatures by Badri (Thermocouples fixed in mold).

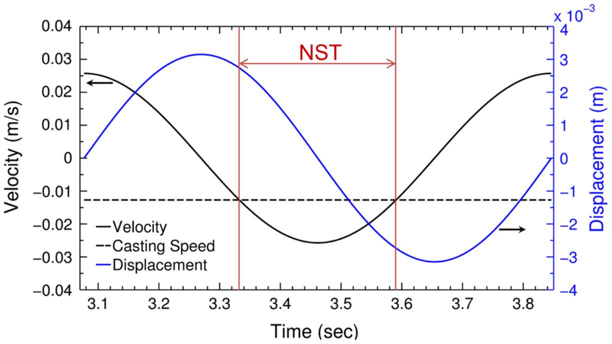

Fig. 18—Displacement, velocity, and NST time over one oscillation for Badri experiment.

ments for hot and cold locations were observed to vary from 0.024 to 0.033 seconds except for the highest value of 0.083 seconds at TC1. Typical averaged model predictions are 0.031 and 0.037 seconds at TC2 and TC3, respectively, while at TC4, the thermocouple that travels below shell tip during oscillations, shows 0.065 seconds lag. The short lag in the model predictions can be seen in Figure 17 between hot and cold locations. These values match very well, considering the extensive variations observed in both the model and the measurements. The lags in both the experiment and the model are shorter than the analytical solution, which suggests that the 2D effects are real.

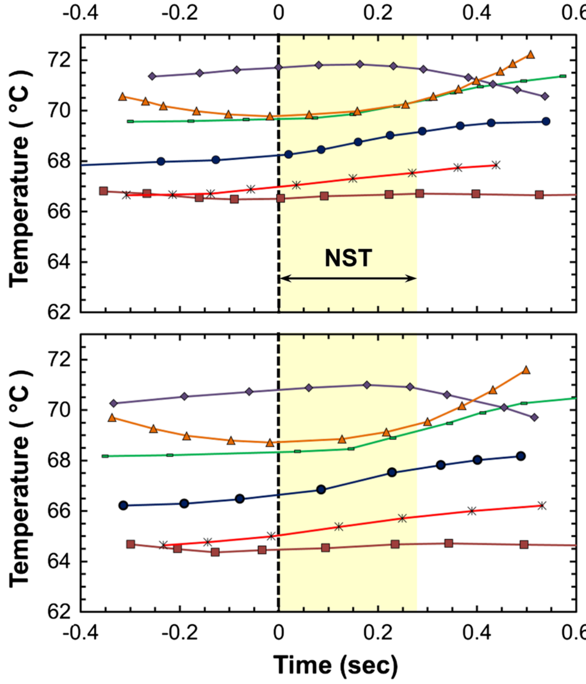

Fig. 19—Badri[96] thermocouple measurements for Trial 31.

G. *Heat Flux Results*

Figure 20 compares the Lagrangian and Eulerian predictions of temperature at TC3 (hot) and adjacent surface heat flux for the Badri case (fifth cycle). As discussed in the previous section, the phase lag is very short relative to the period of the cycle, so the temperature and heat flux rise and fall almost together. As the mold rises above the far-field interface level, the accompanying upward bulging of the meniscus above the shell tip causes local heat flux to increase. The opposite occurs while the mold moves down, as illustrated in Section IV–C. So, in the Eulerian (laboratory) reference frame, heat flux increases during the upstroke and decreases during the downstroke.

The temperature variations of the oscillating thermocouple (Lagrangian reference frame) are much smaller because the heat flux variations over the distances traveled almost match the mold oscillation. However, as the Lagrangian TC moves down with the mold during NST, it is carried closer to the high heat-flux meniscus region and a slight increase is observed in both temperature and heat flux. Badri *et al.*[65] observed that heat flux calculated with a 1D inverse model based on the TC3 temperature history increases during NST and

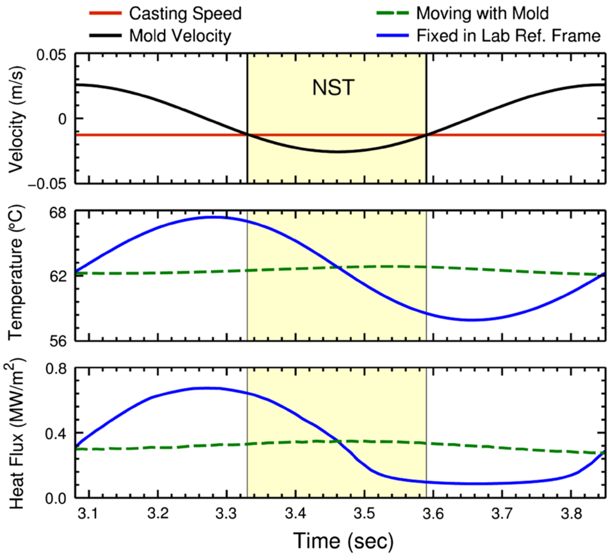

Fig. 20—Comparison between temperature and heat flux predictions at TC3 (hot) location for reference frames fixed in the lab (Eulerian) and mold (Lagrangian) (Badri case).

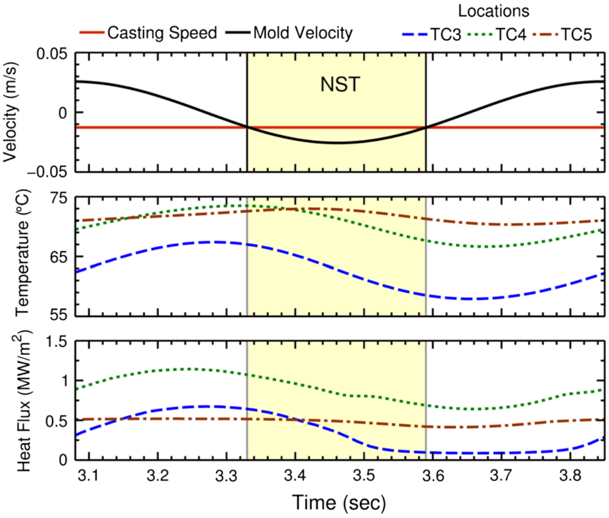

Fig. 21—Temperature and heat flux predictions at TC3–TC5 (hot) locations using lab reference frame (Badri case).

peaks at the end of NST. To maintain the short phase lag between heat flux and temperature, the measured temperature curves for TC3 in Figure 15 should have been shifted slightly left in order to increase during NST. This would also enable a close match with the current model predictions, as well as with the TC3 measurements of Trial 31[96] (Figure 19). Furthermore, the Badri inverse model trend of increasing heat flux during NST for the TC3 history is close to that predicted by the current model (Figure 20), where the heat flux and temperature peaks at TC3 are both toward the end of NST (averaging 66 ± 5 pct and 85 ± 3 pct after start of NST, respectively). Thus, the current model reasonably explains the experimental observations.

Figures 21 and 22 show the Eulerian predictions of temperatures at TC (hot) locations and adjacent heat flux for the Badri (fifth cycle) and Shin (third cycle) cases, respectively, during one cycle. Near the meniscus and shell tip (TC3-4), amplitudes are highest. Farther below the shell tip (TC5-6) they are almost uniform in time. Temperatures near the shell tip generally fall during NST according to the drop in meniscus level, which follows the mold movement, as discussed previously. However, TC5-6 increase during NST for the Shin Case. This is due to overflow of molten steel over the shell tip that occurs during NST, which is not seen in the Badri case simulation.

Figure 23 shows the Lagrangian predictions for TC3-5 (hot) for the Badri case (fifth cycle), which rise and fall as the thermocouples travel up and down with the mold. Above the shell tip (TC3), temperature and heat flux correspond to distance from the slag/steel interface. The minimum distance just after NST (~3.6 seconds) has the highest heat flux and corresponding increase in temperature, as seen in Figure 23 for TC3, which generally matches observations of Badri *et al.*[64] For thermocouples below the shell tip (TC4-5) the predictions vary greatly according to local variations in the thickness profile of the air gap. Specifically, a sudden increase in air-gap resistance at 4 mm below the shell tip causes TC4 heat flux to drop significantly while it is lower than this distance during the downstroke. Similarly, heat flux increases at TC5 when it is close to this distance, during the upstroke. It is important to note from these results that small temperature variations [~2 K (~2 °C)] correspond to large fluctuations in heat flux (0.5 MW/m^2).

Lagrangian predictions for the Shin case are shown in Figure 24 for the second cycle. Thermocouples above the shell tip (TC3) show similar behavior to those in similar locations in the Badri case. Although temperature magnitudes are higher for the Shin case, the amplitudes are lower. This is due to the increase in oscillation frequency, as given by Eq. [33]. The behavior of TC4 is different, however, because overflow occurred near the end of NST during this oscillation cycle. Liquid steel flowed over the shell tip and into the interfacial gap, as illustrated in Figure 25 (for $\alpha_{\mathrm{Fe}} = 0.02$). In reality, this overflowed liquid would solidify and stick to the shell. The mold carries TC4 downward to near the overflow, causing increased heat flux. This naturally produces a temperature increase at TC4, after the expected short phase lag. This matches with Badri's observation of increasing heat flux during NST at location TC3. In the actual experiment by Badri, overflow likely was triggered by the moving meniscus to occur during NST for many successive cycles, resulting in heat flux increasing to a maximum toward the end of NST, at the thermocouple adjacent to the overflow. However, as seen from Figures 17 and 19, many different variations were observed in the measured temperature curves, which suggest that the overflow scenario likely occurs at different times in different experiments or at different oscillation cycles during the same experiment. Since the phenomena are highly transient, this is not surprising. Similar variations are observed in the simulations.

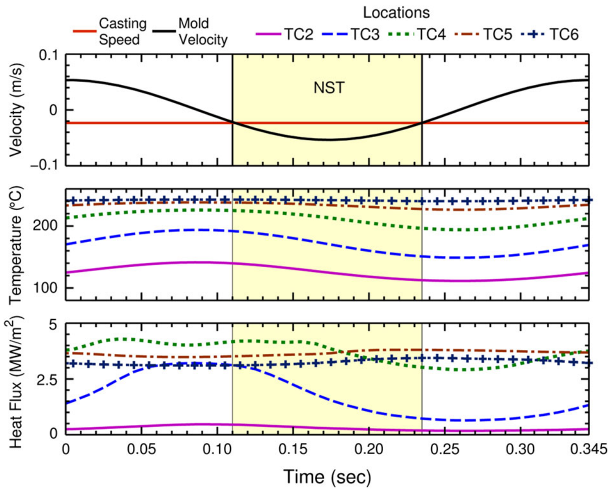

Fig. 22—Temperature and heat flux predictions at TC2–TC6 (hot) locations using lab reference frame (Shin case: 0.77 to 1.12 s).

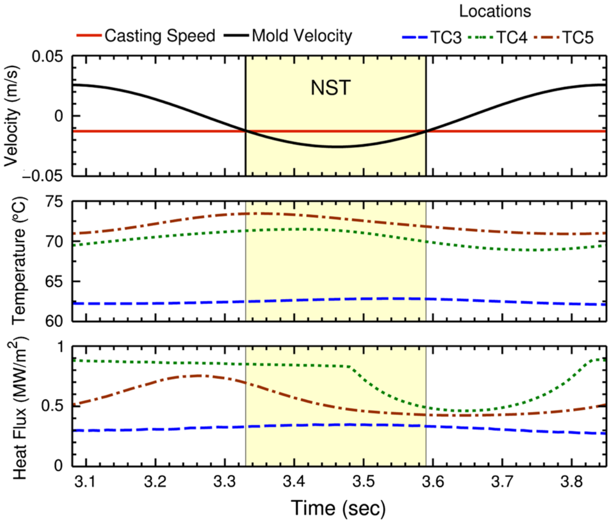

Fig. 23—Temperature and heat flux predictions at TC3–TC6 (hot) locations using mold reference frame (Badri case).

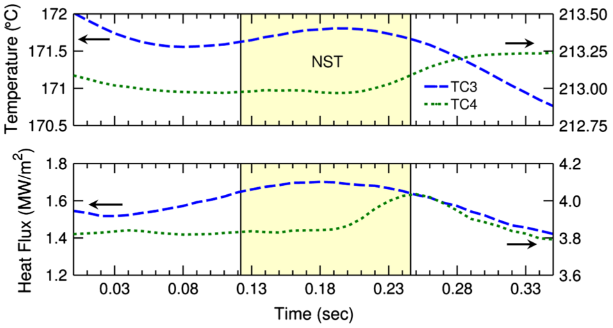

Fig. 24—Temperature and heat flux predictions at TC3-4 (hot) locations using mold reference frame (Shin case: 0.43 to 0.77 s).

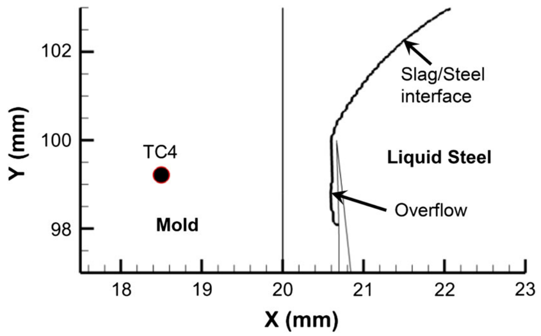

Fig. 25—Overflow event in Shin case (0.59 s).

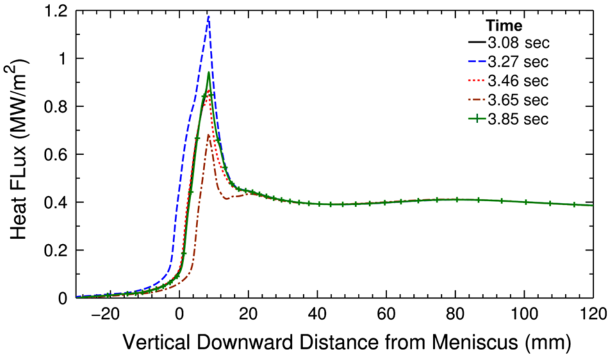

Fig. 26—Predicted transient heat flux profile over an oscillation cycle (Badri case).

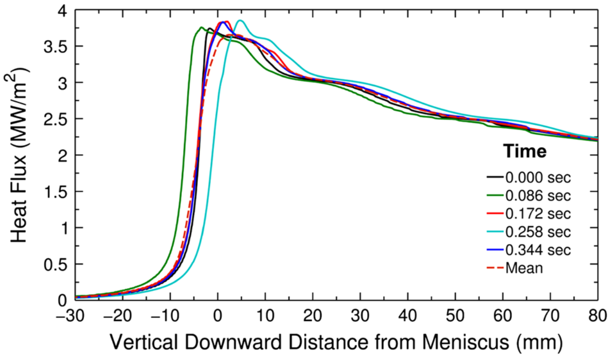

Fig. 27—Predicted transient heat flux profile over an oscillation cycle (Shin case: 0.43 to 0.77 s).

Far below the meniscus, heat flux generally decreases with distance down the mold, owing to increasing gap resistance, which causes heat flux to decrease during NST. In rare locations, an inversion can occur, where heat flux increases with distance, resulting in heat flux increasing very slightly during NST to peak when the mold is lowest, near the end of NST. This situation is given for the current model in further detail elsewhere (Figure 4.21 in Reference 95) and matches observations reported by Lopez *et al.*[60] 45 mm below the meniscus.

Figure 26 shows the vertical heat flux profile at different times during the fifth oscillation cycle for the Badri case. The peak heat flux location is almost constant at 8 mm below the meniscus (far-field steel/slag interface), where the gap resistance is smallest. Large local increases in air-gap profile (below this

Table IV. Casting Conditions, Measured and Predicted Slag Consumption for Validation Cases

						Strip Time		Slag Consumption				
									Predicted			
Case	Slab Width (mm)	Casting Speed (m/min)	Stroke (mm)	Frequency (cpm)	α_m (pct)	NST (s)	PST (s)	Measured (kg/m^2)	g/m s	kg/m^2	g/m cycle	Error (pct)
L1-7	1300	1.490	6.00	174.0	0	0.121	0.224	0.230	5.2001	0.2094	1.7931	−8.96
L1-9	1300	1.466	7.00	125.6	0	0.154	0.324	0.208	5.0992	0.2087	2.4363	0.35
L2-4	1300	1.484	6.47	161.2	24	0.106	0.267	0.238	5.3004	0.2143	1.9727	−9.96
L2-9	1050	1.660	6.77	178.3	24	0.097	0.240	0.194	6.0009	0.2169	2.0191	11.79

α_m, modification ratio.

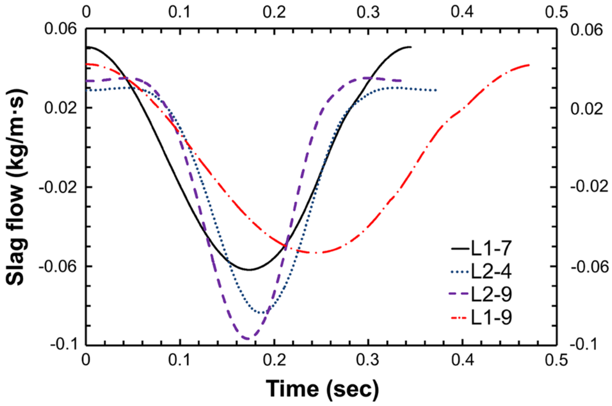

Fig. 28—Predicated transient slag consumption for slag consumption validation cases.

location) and slag thickness (above this location) both cause increased gap resistance that causes the heat flux peak to manifest in this location. The variation of heat flux profile with time 0.5 (0.7 to 1.2) MW/m^2 corresponds to interface oscillation as discussed earlier in Section IV–C. This compares reasonably with the large heat-flux range calculated in this region with a 2D inverse model[99] with the thermocouple temperatures measured by Badri *et al.*[65] In a Lagrangian reference frame, however, the current heat flux varies by only 0.05 (0.3 to 0.35) MW/m^2, as shown on Figure 23. The heat flux measured by Badri's 1D inverse model in this region exhibits large low-frequency variations in addition to high-frequency variations[96] due to oscillation of ~0.06 (0.19 to 0.25) MW/m^2. These variations agree well, and are greatly decreased with the Lagrangian frame.

Figure 27 shows the corresponding vertical heat flux profile for the Shin case (second cycle). In this case, the peak heat flux is less variable during the oscillation cycle because there are no large changes in air-gap profile so gap resistance near the meniscus is more uniform. However, the heat flux peak moves spatially with the mold, according to the interface height variations that accompany the oscillation stroke. In addition, more temporal variation in heat flux is observed below the mold, which corresponds to variations in the gap thickness further down the mold. This heat flux profile and its variations generally match observations in real casters.[10,41,43]

V. PARAMETRIC STUDIES

The validated computational model developed in this work was simplified to increase computational efficiency, and applied in a parametric study to predict slag consumption as a function of different casting variables.

A. *Simplified Model Development*

In a real caster, the solidified slag layer fractures periodically[100] causing effective downward movement at some fraction of the casting speed[41]. Near the meniscus region modeled in this work, however, it is safe to assume that the solid slag moves with the mold (Figure 13). Thus, the mold and solid slag do not contribute to consumption in the current model. Accordingly, the left domain wall was truncated at the solid/liquid interface, as done by Ojeda *et al.*,[57,58] by setting the temperature of this oscillating boundary to 1073 K (800 °C) below the meniscus, to make the viscosity high enough (~10^4 Pa s) to behave as a solid. Above the meniscus, heat flux was set to zero. Different low values of heat flux above the meniscus were investigated and found to have no significant effect.

The gap size for the liquid slag thickness was chosen to match the results of the Shin case, which is observed in Figure 12 to be ~0.6 mm at the solidification temperature of 1073 K (800 °C). The variable cold side shell surface temperature was fixed at ~1794 K (1521 °C), which lowered the viscosity and consequently increased mass flow. To balance this effect, the gap size was reduced to 0.5 mm to match the slag consumption of the Shin case. Most of the domain is modeled with the properties of melting slag. The 10 mm wide region next to the 1073 K (800 °C) left wall was given solidification properties. After a mesh independence study, a mesh of 5340 cells was chosen for this model.

B. *Simplified Model Validation*

The simplified model was first applied to four different sets of casting conditions (Table IV) with available consumption measurements from POSCO trials in 2002 and 2003 from Shin.[19] Figure 28 compares the varying slag consumptions for the four cases during a typical oscillation cycle.

The predicted and measured consumptions are compared in Table IV, and agree within 11 pct. This error seems reasonable, considering the uncertainty in measuring bags

Table V. Casting Conditions, Measured and Predicted Slag Consumption for Parametric Study Cases

					Strip Time		Predicted Slag Consumption		
Case	Casting Speed (mm/s)	Stroke (mm)	Frequency (cpm)	α_m* (pct)	Negative (s)	Positive (s)	g/m s	kg/m^2	g/m cycle
C-1	**23.30**	7.00	125.6	0	0.158	0.319	4.91	0.211	2.345
C-2	**24.30**	7.00	125.6	0	0.154	0.324	5.10	0.210	2.437
C-3	**25.30**	7.00	125.6	0	0.150	0.327	5.28	0.209	2.522
S-1	24.80	**5.00**	174.0	0	0.109	0.236	5.16	0.208	1.780
S-2	24.80	**6.00**	174.0	0	0.121	0.224	5.18	0.209	1.786
S-3	24.80	**7.00**	174.0	0	0.129	0.216	5.26	0.212	1.814
F-1	24.30	7.00	**105.6**	0	0.161	0.408	5.07	0.209	2.880
F-2	24.30	7.00	**125.6**	0	0.154	0.324	5.10	0.210	2.437
F-3	24.30	7.00	**145.6**	0	0.144	0.268	5.14	0.212	2.118
F-4	24.30	7.00	**165.6**	0	0.133	0.229	5.19	0.214	1.881
F2-1	24.80	6.00	**104.0**	0	0.130	0.447	5.22	0.211	3.012
F2-2	24.80	6.00	**134.0**	0	0.134	0.314	5.09	0.205	2.279
F2-3	24.80	6.00	**174.0**	0	0.121	0.224	5.18	0.209	1.786
M-1	24.70	6.47	161.2	**0**	0.130	0.242	5.17	0.209	1.924
M-2	24.70	6.47	161.2	**12**	0.117	0.255	5.22	0.211	1.943
M-3	24.70	6.47	161.2	**24**	0.105	0.267	5.29	0.214	1.969

*α_m = modification ratio.

of powder, and the model assumptions of constant gap size (0.5 mm) and neglect of the OM shape on consumption.

C. *Casting Conditions for Parametric Studies*

To study the effects of casting speed, stroke, frequency, and modification ratio on slag consumption, four sets of simulations were conducted, (16 cases total) for conditions given in Table V. In each set of cases, (C, S, F, and M) one parameter is changed (marked in bold) while others are kept constant. Mold slag consumption (kg/min or bags per hour), is quantified in three different ways: (1) a total rate of mass per unit time per unit length of strand perimeter (g/m s), (2) mass per oscillation cycle per unit length of strand perimeter (g/m cycle), or (3) mass per unit area of strand surface (kg/m^2). The latter correlates best with liquid layer thickness in the gap and lubrication in practice, so is reported here unless specified otherwise.

D. *Results*

1. *Casting Speed (v_c)*

The predicted mean slag consumption (kg/m^2) decreases slightly with increasing casting speed, as shown in Table V, Case C1-3 and in Figure 29(a). Specifically, an 8.6 pct increase in casting speed (from 23.3 to 25.3 mm/s) causes the slag consumption rate (g/m s or g/m cycle) to increase by only 7.5 pct, which corresponds to a decrease in slag consumption of 1 pct. This relationship is well documented in previous measurements,[19,20,47,48] including casters with both sinusoidal and non-sinusoidal oscillation.[46]

2. *Stroke (s)*

Based on Case S1-3 in Table V, Figure 29(a) shows that consumption (kg/m^2) increases slightly with increase of stroke. Increasing stroke by 40 pct increases

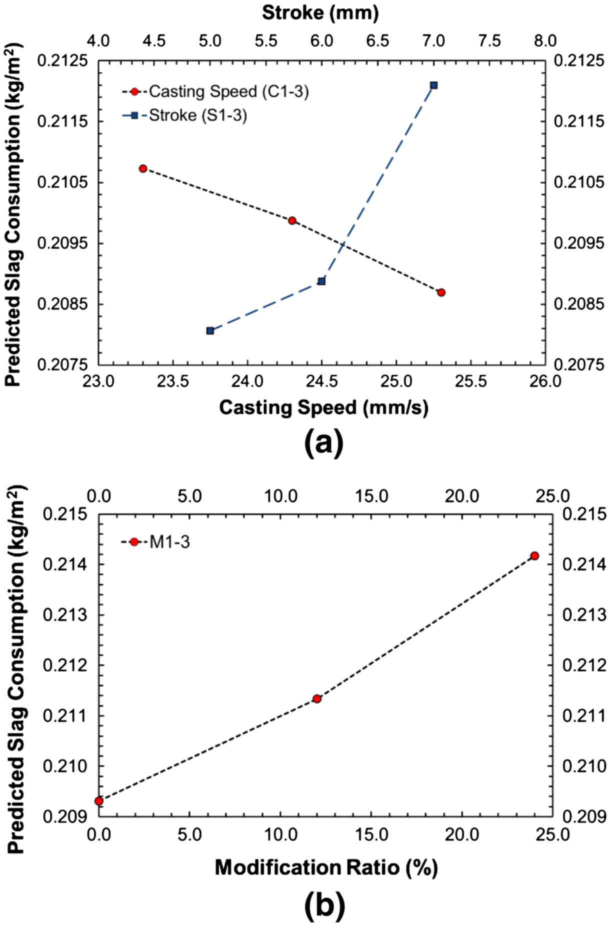

Fig. 29—Predicted effect of changing casting speed, stroke and modification ratio on slag consumption.

consumption by only 2 pct, however, this agrees with previous measurements, such as quantified with the empirical equation of Tsutsumi *et al.*,[46]

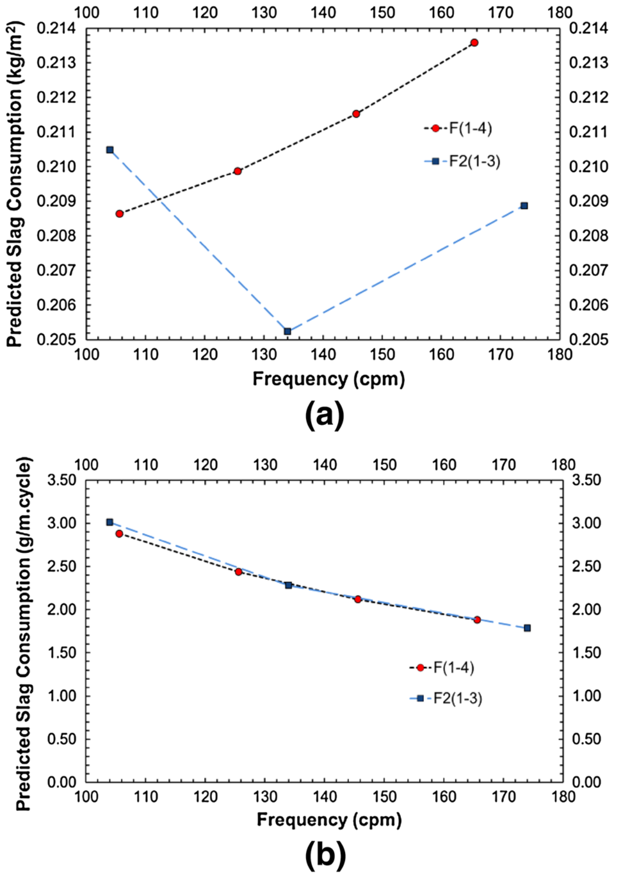

Fig. 30—Predicted effect of changing frequency on slag consumption.

$$Q = \frac{k_\beta}{T_{\mathrm{cs}}\sqrt{\mu}}\frac{s^{0.4}}{v_{\mathrm{c}}}\cos^{-1}\left(-\frac{1000 \times v_{\mathrm{c}}}{2\pi f s}\right), \qquad [34]$$

where Q is slag consumption (kg/m^2), v_{c} is casting speed (m/min), f is frequency (cpm), s is stroke (mm), μ is viscosity at 1573 K (1300 °C) (P), T_{cs} is crystallization temperature (°C) and k_β is constant. In Eq. [34], stroke appears in two places with opposite effects. The net effect of increasing stroke is a slight increase of all three measures of consumption: (g/m s, g/m cycle, and kg/m^2).

3. *Frequency (f)*

Two sets of simulations with two different strokes (F1-4, F2-1-3) were done to study the effect of changing frequency. Frequency has small inconsistent effect on slag consumption (kg/m^2) as shown in Figure 30(a). Increasing frequency by ~62 pct causes only 1 to 2 pct variation (both decrease and increase) although it decreases slag consumption per cycle (g/m cycle) by ~35 pct, as shown in Figure 30(b) for both F1-4 and F2-1-3. This agrees with empirical equations by many researchers[46,52,101,102] as reviewed by Saraswat *et al.*[103] that show both increasing and decreasing slag consumption per unit area. The inverse relationship with consumption per cycle (g/m cycle) agrees with Shin's[19] equation.

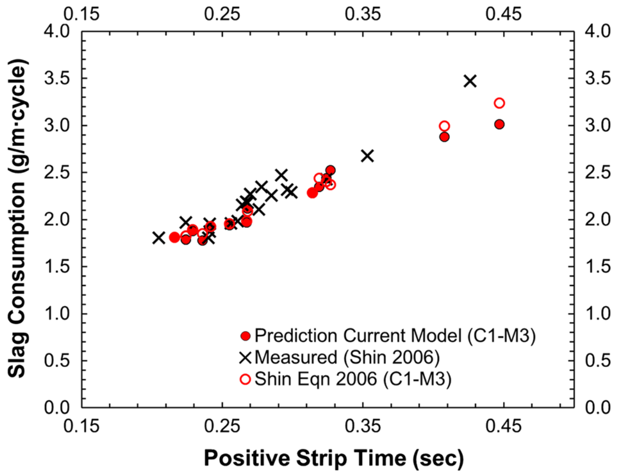

Fig. 31—Predicted and measured[74] slag consumption *vs* positive strip time.

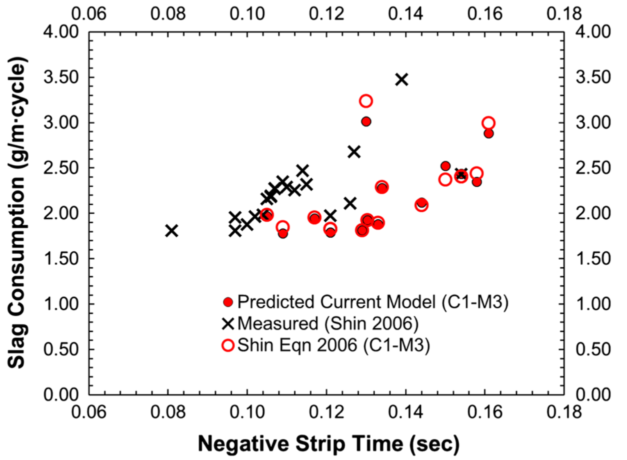

Fig. 32—Predicted and measured[74] slag consumption *vs* negative strip time.

4. *Modification Ratio (α_m)*

The effect of non-sinusoidal oscillation was investigated with two casting conditions (M2-3) using 12 and 24 pct modification ratio (α_{m}) which is defined after Eq. [20]. Increasing α_{m} to 24 pct is predicted to increase slag consumption by ~2.4 pct, as shown in Figure 29(b). This trend agrees quantitatively with many previous measurements.[4,19] Tsutsumi *et al.*,[46] measured over 50 pct higher consumption and explained this trend is due to the increase in PST that accompanies the increase of α_{m}. Suzuki *et al.*[4] reported that this trend is due to decreasing frictional force. Finally, the relative speed of the mold to the solidified shell is higher during NST with non-sinusoidal oscillation.

5. *Positive Strip Time (PST, t_p)*

To combine the effect of all four independent variables (casting speed, frequency, modification ratio, and stroke) into one variable, many researchers[4,19,46,104,105] suggest using PST (t_{p}) and find a strong correlation of slag consumption per cycle increasing with increasing t_{p}. All 16 simulations in the current study are plotted with t_{p} in Figure 31, which shows this expected trend. The corresponding predictions using the empirical equation of Shin *et al.*[19] for the 16 simulation conditions are presented in the same figure, as well as his original slag consumption measurements obtained for different conditions. A very good match and a strong correlation with t_{p} are observed.

6. *Negative Strip Time (NST, t_n)*

Like PST, another popular indicator of slag consumption is NST (t_{n}). Several researchers[8,106,107] report slag consumption per cycle increases with t_{n}. Figure 32 plots the predicted slag consumption of the current study with t_{n} for Cases C1-M3, together with predictions by Shin *et al.*'s[19] equation and original slag consumption measurements. Although an increasing trend is observed with t_{n}, it is not as prominent as the relation with t_{p}.

VI. CONCLUSIONS

The current work presents a computational model to predict thermal-flow behavior near the meniscus during an oscillation cycle and slag consumption in continuous steel casting. Both time-averaged and transient predictions match reasonably with lab experiments, plant measurements, and literature. The following conclusions can be drawn:

1. The slag/liquid–steel interface follows the mold movement closely. The meniscus moves upward during the up stroke and is pushed downward during the down stroke by the slag rim.
2. Variations in mold temperatures and heat flux near the meniscus are higher than far above or below. The variations decrease for higher frequency mold oscillation.
3. Temperatures evolve differently in Eulerian and Lagrangian reference frames. The real mold thermocouples (Lagrangian) experience less variation in temperature [~1 K (~1 °C)] near meniscus for commercial caster than do mold wall locations fixed in space (Eulerian), because their oscillating movement follows the oscillating interface.
4. Overflow greatly affects the temperature/heat flux distribution during a cycle. With no overflow, in the Lagrangian reference frame, the model predicts oscillating heat flux that increases to a maximum during NST for thermocouples near meniscus and shell tip. But, when overflow occurs, the predicted heat flux increases to a maximum near the end of NST, as observed in both the lab experiment and simulations. The transient behavior during a cycle may differ according to when or if overflow occurs, but the time averages should be similar.
5. Below the meniscus region, heat flux tends to decrease with distance down the mold, so during the downstroke (NST) of each cycle, the heat flux tends to decrease.
6. The oscillating mold wall drags slag downward in the gap between the mold hot face and the steel shell mainly during NST. This slag consumption is assisted by the pressure generated by the oscillating slag rim that pumps liquid slag into the gap at the meniscus near the end of NST.
7. Transient slag consumption prediction closely follows the oscillation velocity of the mold. Part of the time period, slag flows up into the channel and it moves downward in the rest of it. The net result is a constant downward slag flow rate per oscillation cycle. Predicted mean slag consumption matches measurements with in ±11 pct.
8. Increase of casting speed (8.6 pct) increases slag consumption rate (kg/min or g/m cycle) (7.5 pct) which results in a slight decrease in slag consumption per unit strand area (kg/m^2) (1 pct).
9. Increase of stroke length and modification ratio increases slag consumption slightly.
10. While a consistent relationship is not found between frequency and slag consumption per unit area (kg/m^2), a strong inverse trend is found with slag consumption per unit length per cycle (g/m cycle), decreasing 35 pct with a ~62 pct increase in frequency.
11. Slag consumption (g/m cycle) increases with increasing both PST and NST. The relation with PST is more clear.

ACKNOWLEDGMENTS

This work was supported by the Continuous Casting Consortium at the University of Illinois at Urbana-Champaign (UIUC). The authors thank Prof. Dr. Alan Cramb for providing clarification of Badri's thesis. The authors extend special gratitude to Claudio Ojeda, former Visiting Scholar at UIUC, for conducting substantial initial work on this project.

APPENDIX

See Appendix Tables A1 and A2.

Table A1. Input Data for Steady-State CON1D Model Cases

Parameters	Shin Case	Badri Case	Unit
Carbon content, C	0.003	0.0046	pct
Liquidus temperature, T_{liq}	1806.82 (1533.82)	1804.87 (1531.87)	K (°C)
Solidus temperature, T_{sol}	1791.15 (1518.15)	1791.7 (1518.7)	K (°C)
Fraction solid for shell thickness location, f_s	0.5	0.3	
Mold thickness at top (including water channel)	40	22.23	mm
Total mold length, $Z_{\text{mold\_total}}$	900	451	mm
Total mold width	1300	100	mm
Initial cooling water temperature, T_{water}	323 (50)	311 (38)	K (°C)
Water channel geometry,			mm
Depth, d_{ch}	20	13.7	
Width, w_{ch}	5	7.9	
Spacing between channels, l_{ch}	19	15.8	
Total channel cross section area, W/N	7290/900	647.21	mm^2
Cooling water velocity, V_{water}	-10.22	-8	m/s
Mold conductivity, k_{mold}	350	340	W/m K
Mold emissivity, $\varepsilon_{\text{mold}}$	0.5	0.5	
Mold powder solidification temperature, T_{fsol}	1374 (1101)	1374 (1101)	K (°C)
Mold powder conductivity, $k_{\text{solid}}/k_{\text{liquid}}$	1.5/1.5	1/0.85	W/m K
Air conductivity, k_{air}	0.06	0.06	W/m K
Slag layer/mold resistance, r_{contact}	5.00E$-$09	5.00E$-$09	m^2 K/W
Mold powder viscosity at 1573 K (1300 °C), μ_{1300}	5.5	5.5	Poise
Exponent for temperature dependent viscosity, n	1.8	1.8	
Slag density, ρ_{slag}	2600	2600	kg/m^3
Slag absorption factor, a	250	250	
Slag emissivity, $\varepsilon_{\text{slag}}$	0.9	0.9	
Mold powder consumption rate, Q_{slag}	0.236	1.23	kg/m^2
Empirical solid slag layer speed factor, f_v	0	0.005	
Casting speed, v_c	0.0232	0.0127	m/s
Pour temperature, T_{pour}	1838 (1565)	1805 (1532)	K (°C)
Slab geometry, $W \times N$	1300 × 230	400 × 100	mm
Nozzle submergence depth, d_{nozzle}	161	100	mm
Oscillation mark geometry, $d_{\text{mark}} \times w_{\text{mark}}$	0.25 × 3	0.81 × 8.73	mm
Mold oscillation frequency, f	2.9	1.3	Hz
Oscillation stroke, stroke	5.89	6.3	mm
Coating layer, Ni	1 to 1.4	0.05	mm
Coating layer, Cr	0.1	—	mm
Scale	—	0.02	mm
Air gap	—	0.10 to 0.21	mm

Table A2. Steel Composition

Case\Components	C	Mn	S	P	Si	Cr	Ni	Cu	Ti	Al	N	Mo	V	Nb
Shin case (pct)	0.003	0.08	0.01	0.015	0.005	0.01	0.01	0.01	0.05	0.04	—	—	—	—
Badri case (pct)	0.0046	0.46	0.0089	0.011	0.1	0.035	0.015	0.027	0.015	0.051	0.0057	0.004	0.003	0.0002

REFERENCES

1. B.G. Thomas, M.S. Jenkins, and R.B. Mahapatra: *Ironmak. Steelmak.*, 2004, vol. 31, pp. 485–94.
2. B.G. Thomas: *Iron Steel Technol.*, 2006, vol. 3, p. 127.
3. K.C. Mills and A.B. Fox: *ISIJ Int.*, 2003, vol. 43, pp. 1479–86.
4. M. Suzuki, H. Mizukami, T. Kitagawa, K. Kawakami, S. Uchida, and Y. Komatsu: *ISIJ Int.*, 1991, vol. 31, pp. 254–61.
5. T. Nakano, K. Nagano, N. Masuo, M. Fuji, and T. Matsuyama: *Nippon Steel Tech. Rep.*, 1987, vol. 34, pp. 21–30.
6. T. Tanaka and K. Takatani: *CAMP-ISIJ*, 1989, vol. 2, p. 1263.
7. H. Sha, R. Diedrichs, and K. Schwerdtfeger: *Metall. Mater. Trans. B*, 1996, vol. 27B, pp. 305–14.
8. C. Perrot, J.N. Pontoire, C. Marchionni, M.-R. Ridolfi, and L.F. Sancho: *Metall. Res. Technol.*, 2005, vol. 102, pp. 887–96.
9. R.B. Mahapatra, J.K. Brimacombe, and I.V. Samarasekera: *Metall. Trans. B*, 1991, vol. 22B, pp. 875–88.
10. E. Takeuchi and J.K. Brimacombe: *Metall. Trans. B*, 1984, vol. 15B, pp. 493–509.
11. K.C. Mills, A. Olusanya, R. Brooks, R. Morrell, and S. Bagha: *Ironmak. Steelmak.*, 1988, vol. 15, pp. 257–64.
12. R.B. McDavid: Thesis, University of Illinois at Urbana-Champaign, 1990.
13. K.C. Mills, T.J.H. Billany, A.S. Normanton, B. Walker, and P. Grieveson: *Ironmak. Steelmak.*, 1991, vol. 18, pp. 253–65.
14. T.J.H. Billany, A.S. Normanton, K.C. Mills, and P. Grieveson: *Ironmak. Steelmak.*, 1991, vol. 18, pp. 403–10.
15. S. Hiraki, K. Nakajima, T. Murakami and T. Kanazawa: *77th Steelmaking Conference*, ed. ISS/AIME, Chicago, IL, 1994, pp. 397–403.
16. J. Konishi, M. Militzer, J.K. Brimacombe, and I.V. Samarasekera: *Metall. Mater. Trans. B*, 2002, vol. 33B, pp. 413–23.
17. L. Hibbeler and B.G. Thomas: *AISTech Steelmaking Conference Proceedings*, 2010.
18. R. Bommaraju, R. Glennon, and M. Frazee: *1st European Conference on Continuous Casting*, Florence, Italy, 1991, pp. 1.599–1.610.

19. H.-J. Shin, S.H. Kim, B.G. Thomas, G.G. Lee, J.M. Park, and J. Sengupta: *ISIJ Int.*, 2006, vol. 46, pp. 1635–44.
20. H. Nakato, T. Sakuraya, T. Nozaki, T. Emi and H. Nishikawa: *Steelmaking Proceedings*, Washington, DC, 1986, pp. 137–43.
21. A. Delhalle, M. Larrecq, J.F. Marioton and P.V. Riboud: *Steelmaking Proceedings*, Washington, DC, 1986, pp. 145–52.
22. W. Jander: *Z. Anorg. Allg. Chem.*, 1927, vol. 163, pp. 1–30.
23. E. Anzai, T. Shigezumi, T. Nakano, T. Ando, and M. Ikeda: *Nippon Steel Tech. Rep.*, 1987, vol. 34, pp. 31–40.
24. K. Schwerdtfeger and H. Sha: *Metall. Mater. Trans. B*, 2000, vol. 31B, pp. 813–26.
25. K. Okazawa, T. Kajitani, W. Yamada, and H. Yamamura: *ISIJ Int.*, 2006, vol. 46, pp. 226–33.
26. K. Okazawa, T. Kajitani, W. Yamada, and H. Yamamura: *ISIJ Int.*, 2006, vol. 46, pp. 234–40.
27. A. Yamauchi, T. Emi, and S. Seetharaman: *ISIJ Int.*, 2001, vol. 42, pp. 1084–93.
28. G.J.W. Kor: *2nd Process Technology Conference*, Chicago, IL, 1981, pp. 124–32.
29. D.R. Bland: *J. Inst. Math. Appl.*, 1984, vol. 32, pp. 89–112.
30. N. Fowkes and A. Woods: Unpublished research, 1989.
31. J.M. Hill, Y.H. Wu, and B. Wiwatanapataphee: *J. Eng. Math.*, 1999, vol. 36, pp. 311–26.
32. J.R. King, A.A. Lacey, C.P. Please, P. Wilmott, and A. Zoryk: *Math. Eng. Ind.*, 1993, vol. 4, pp. 91–106.
33. A.W. Cramb and F.J. Mannion: *Steelmaking Proceedings*, Detroit, MI, 1985, pp. 349–59.
34. H. Steinruck and C. Rudischer: *Fifth World Congress on Computational Mech*anics, 2002.
35. Y. Meng and B.G. Thomas: *Metall. Mater. Trans. B*, 2003, vol. 34B, pp. 685–705.
36. J. Sengupta, B.G. Thomas, and M.A. Wells: *Metall. Mater. Trans. A*, 2005, vol. 36A, pp. 187–204.
37. J. Sengupta, M.-K. Trinh, D. Currey, and B.G. Thomas: *AISTech Steelmaking Conference Proceedings*, 2009, pp. 4–7.
38. J. Iwasaki and B.G. Thomas: *Supplemental Proceedings: Materials Properties, Characterization, and Modeling*, TMS, Hoboken, NJ, 2012, pp. 355–62.
39. B. Santillana, L.C. Hibbeler, B.G. Thomas, A. Hamoen, A. Kamperman, and W. Van der Knoop: *ISIJ Int.*, 2008, vol. 48, pp. 1380–88.
40. Y. Meng, C. Li, J. Parkman and B.G. Thomas: *TMS Annual Meeting-Solidification Processes and Microstructures Symposium*, Charlotte, NC, 2004, pp. 33–39.
41. Y. Meng and B.G. Thomas: *ISIJ Int.*, 2006, vol. 46, pp. 660–69.
42. B. Petrus, K. Zheng, X. Zhou, B.G. Thomas, and J. Bentsman: *Metall. Mater. Trans. B*, 2011, vol. 42B, pp. 87–103.
43. L.C. Hibbeler, B.G. Thomas, R.C. Schimmel, and G. Abbel: *Metall. Mater. Trans. B*, 2012, vol. 43B, pp. 1156–72.
44. B.G. Thomas and Y. Meng: *CONID Users Manual*, University of Illinois, 2002.
45. S. Ogibayashi, T. Mukai, and Y. Mimura: *Nippon Steel Tech. Rep.*, 1987, vol. 34, pp. 1–10.
46. K. Tsutsumi, H. Murakami, S.I. Nishioka, M. Tada, M. Nakada, and M. Komatsu: *Trans. Iron Steel Inst. Jpn.*, 1998, vol. 84, pp. 617–24.
47. M. Suzuki, M. Suzuki, and M. Nakada: *ISIJ Int.*, 2001, vol. 41, pp. 670–82.
48. M. Kawamoto, T. Murakami, M. Hanao, H. Kikuchi, and T. Watanabe: *Ironmak. Steelmak.*, 2002, vol. 29, pp. 199–202.
49. M.M. Wolf: *Steelmaking Conference*, Washington, DC, 1991, pp. 51–71.
50. M. Bobadilla, J.M. Jolivet, J.Y. Lamant, and M. Larrecq: *Mater. Sci. Eng. Proc. Conf.*, 1993, vol. 173, pp. 275–85.
51. T. Darle, A. Mouchette, M. Roscini, M. Nadif, and D. Salvadori: *76th Steelmaking Conference*, 1993, pp. 209–18.
52. O.D. Kwon, J. Choi, I.R. Lee, J.W. Kim, K.H. Moon, and Y.K. Shin: *Steelmaking Conference Proceedings*, Washington, DC, 1991, pp. 561–68.
53. R.M. McDavid and B.G. Thomas: *Metall. Mater. Trans. B*, 1996, vol. 27B, pp. 672–85.
54. B. Zhao, S.P. Vanka, and B.G. Thomas: *Int. J. Heat Fluid Flow*, 2005, vol. 26, pp. 105–18.
55. R. Chaudhary, B.G. Thomas, and S.P. Vanka: *Metall. Mater. Trans. B*, 2012, vol. 43B, pp. 532–53.
56. R. Liu, B.G. Thomas, and J. Sengupta: *IOP Conf. Ser. Mater. Sci. Eng.*, 2012, vol. 33, p. 012015.
57. C. Ojeda, J. Sengupta, B.G. Thomas, J. Barco, and J.L. Arana: *AISTech Iron and Steel Technology Conference*, Cleveland, OH, 2006, pp. 1017–28.
58. C. Ojeda, B.G. Thomas, J. Barco and J.L. Arana: *AISTech 2007—Iron and Steel Technology Conference*, May 7–10 2007, Indianapolis, IN, 2007, pp. 269–83.
59. J. Sengupta, B.G. Thomas, H.-J. Shin, G.-G. Lee, and S.-H. Kim: *Metall. Mater. Trans. A*, 2006, vol. 37A, pp. 1597–1611.
60. P.E. Ramirez Lopez, K.C. Mills, P.D. Lee, and B. Santillana: *Metall. Mater. Trans. B*, 2012, vol. 43B, p. 109.
61. P.E. Ramirez-Lopez, P.D. Lee, and K.C. Mills: *ISIJ Int.*, 2010, vol. 50, pp. 425–34.
62. C.W. Hirt and B.D. Nichols: *J. Comput. Phys.*, 1981, vol. 39, pp. 201–25.
63. V.R. Voller and C. Prakash: *Int. J. Heat Mass Transfer*, 1987, vol. 30, pp. 1709–19.
64. A. Badri, T.T. Natarajan, C.C. Snyder, K.D. Powers, F.J. Mannion, M. Byrne, and A.W. Cramb: *Metall. Mater. Trans. B*, 2005, vol. 36B, pp. 373–83.
65. A. Badri, T.T. Natarajan, C.C. Snyder, K.D. Powers, F.J. Mannion, and A.W. Cramb: *Metall. Mater. Trans. B*, 2005, vol. 36B, pp. 355–71.
66. J.U. Brackbill, D.B. Kothe, and C. Zemach: *J. Comput. Phys.*, 1992, vol. 100, pp. 335–54.
67. M. Ishii: *Thermo-fluid Dynamic Theory of Two-Phase Flow*, Eyrolles, Paris, 1975.
68. F.R. Menter: *AIAA J.*, 1994, vol. 32, pp. 1598–1605.
69. F.R. Menter, M. Kuntz, and R. Langtry: *Turbul. Heat Mass Transfer*, 2003, vol. 4, pp. 625–32.
70. ANSYS Fluent. 13.0, Canonsburg, PA, 2013.
71. Y.M. Won and B.G. Thomas: *Metall. Mater. Trans. A*, 2001, vol. 32A, pp. 1755–67.
72. C.A. Sleicher and M.W. Rouse: *Int. J. Heat Mass Transfer*, 1975, vol. 18, pp. 677–683.
73. Y. Meng, B.G. Thomas, A.A. Polycarpou, A. Prasad, and H. Henein: *Can. Metall. Q.*, 2006, vol. 45, pp. 79–94.
74. H.-J. Shin: Thesis, Pohang University of Science and Technology, 2006.
75. P.V. Riboud, Y. Roux, L.D. Lucas, and H. Gaye: *Fachberichte Huttenpraxis Metallweiterverarbeitung*, 1981, vol. 19, pp. 859–69.
76. K. Koyama, Y. Nagano, K. Nagano, and T. Nakano: *Nippon Steel Tech. Rep.*, 1987, vol. 34, pp. 41–47.
77. T. Iida, H. Sakai, Y. Kita, and K. Murakami: *High Temp. Mater. Process.*, 2000, vol. 19, p. 153.
78. K.C. Mills and S. Sridhar: *Ironmak. Steelmak.*, 1999, vol. 26, pp. 262–68.
79. M.D. Lanyi and C.J. Rosa: *Metall. Trans. B*, 1981, vol. 12B, pp. 287–98.
80. D. Larson: *Ind. Heat.*, 1986, vol. 53, pp. 16–17.
81. K. Rietema: *The Dynamics of Fine Powders*, Elsevier, London, 1991, p. 9.
82. R. Taylor and K.C. Mills: *Ironmak. Steelmak.*, 1988, vol. 15, pp. 187–194.
83. J.K. Mackenzie and R. Shuttleworth: *Proc. Phys. Soc. Lond. B*, 1949, vol. 62, p. 833.
84. R. Eriksson and S. Seetharaman: *Metall. Mater. Trans. B*, 2004, vol. 35B, pp. 461–69.
85. H. Hasegawa, H. Ohta, H. Shibata, and Y. Waseda: *High Temp. Mater. Proc.*, 2012, vol. 31, pp. 299-673.
86. M. Kishimoto, M. Maeda, and Y. Kawai: *J. Met.*, 1984, vol. 36, pp. 93–93.
87. A.W. Cramb and I. Jimbo: *Iron Steelmak.*, 1989, vol. 16, pp. 43–55.
88. J. Lee and K. Morita: *ISIJ Int.*, 2002, vol. 42, pp. 588–94.
89. B.J. Keene: *Int. Mater. Rev.*, 1993, vol. 38, pp. 157–192.
90. A. Kasama, A. McLean, W.A. Miller, Z. Morita, and M.J. Ward: *Can. Metall. Q.*, 1983, vol. 22, pp. 9–17.
91. K.C. Mills and Y.C. Su: *Int. Mater. Rev.*, 2006, vol. 51, pp. 329–51.
92. T. Young: *Philos. Trans. R. Soc. Lond.*, 1805, vol. 95, pp. 65–87.
93. H. Nakato and I. Muchi: *Tetsu-to-Hagane*, 1980, vol. 66, pp. 33–42.

94. J.J. Bikerman: *Physical Surfaces*, Academic Press, New York, 1970, pp. 11–12.
95. ASM Jonayat: Thesis, University of Illinois at Urbana-Champaign, 2014.
96. A. Badri: Thesis, Carnegie Mellon University, Pittsburgh, PA, 2003.
97. N. Ozisik: *Inverse Heat Transfer: Fundamentals and Applications*, Taylor & Francis, New York, 2000.
98. J.V. Beck, B. Blackwell, and C.R.S. Clair: *Inverse Heat Conduction: Ill-Posed Problems*, Wiley, New York, 1985.
99. B.G. Thomas, M.A. Wells, and D. Li: *Monitoring of Meniscus Thermal Phenomena with Thermocouples in Continuous Casting of Steel*, Wiley, New York, 2011.
100. R.J. O'Malley and J. Neal: *Proceedings of METEC Congress*, Dusseldorf, Germany, 1999.
101. H. Maeda and T. Hirose: *CAMP-ISIJ*, 1993, pp. 280.
102. M. Wolf: *Conference on Continuous Casting of Steel in the Developing Countries*, Beijing, China, 1993, pp. 66–76.
103. R. Saraswat, A.B. Fox, K.C. Mills, P.D. Lee, and B. Deo: *Scand. J. Metall.*, 2004, vol. 33, pp. 85–91.
104. H. Mizukami, K. Kawakami, and T. Kitagawa: *Trans. Iron Steel Inst. Jpn.*, 1986, vol. 72, pp. 1862–69.
105. K. Kawakami, T. Kitagawa, H. Mizukami, H. Uchibori, S. Miyahara, M. Suzuki, and Y. Shiratani: *Tetsu-to-Hagane*, 1981, vol. 67, pp. 1190–99.
106. H. Shin, G. Lee, W. Choi, S. Kang, S. Kim, J. Park, and B.G. Thomas: *AISTech Conference Proceedings*, 2004, pp. 1157.
107. K. Hamagami, K. Sorimachi, M. Kuga, T. Koshikawa and M. Saigusa: *Steelmaking Conference*, 1982, pp. 358–64.